Real Time Computational Algorithms for Eddy Current Based Damage Detection

H. T. Banks †, Michele L. Joyner †, Buzz Wincheski ‡, and William P. Winfree ‡

†Center for Research in Scientific Computation, North Carolina State University, Raleigh, NC 27695

‡NASA Langley Research Center, Hampton, VA 23681

Abstract. In the field of nondestructive evaluation, new and improved techniques are constantly being sought to facilitate the detection of hidden corrosion and flaws in structures such as airplanes and pipelines. In this paper, we explore the feasibility of detecting such damages by application of an eddy current based technique coupled with reduced order modeling.

We begin by developing a model for a specific eddy current method in which we make some simplifying assumptions reducing the three-dimensional problem to a two-dimensional problem. (We do this for proof-of-concept.) Theoretical results are then presented which establish the existence and uniqueness of solutions as well as continuous dependence of the solutions on the parameters which represent the damage. We further discuss theoretical issues concerning the least squares parameter estimation problem used in identifying the geometry of the damage.

To solve the identification problem, an optimization algorithm is employed which requires solving the forward problem numerous times. To implement these methods in a practical setting, the forward algorithm must be solved with extremely fast and accurate solution methods. In constructing these computational methods, we employ reduced order Proper Orthogonal Decomposition (POD) techniques. This approach permits one to create a set of basis elements spanning a data set consisting of either numerical simulations or experimental data. We discuss two different algorithms for forming the POD approximations, a POD/Galerkin technique and a POD/Interpolation technique.

Finally, results of the inverse problem associated with damage detection are given using both simulated data with relative noise added as well as experimental data obtained using a giant magnetoresistive (GMR) sensor. The experimental results are based on successfully using experimental data to form the POD basis elements (instead of numerical simulations), thus illustrating the effectiveness of this method on a wide range of applications. In both instances the methods are found to be efficient and robust. Moreover, the methods were fast; our findings demonstrate a *significant* reduction in computational time.

1. Introduction

Nondestructive evaluation (NDE) is the process of examining a material or article without impairing its future usefulness. NDE is sometimes referred to as nondestructive testing (NDT) or nondestructive inspection (NDI), although there may be subtle differences in their definitions depending on the author. For the purposes of this paper, however, we will use the terminology interchangeably.

The process of examining a material using nondestructive evaluation techniques is not new but is becoming increasingly important as technology continually advances. According to the American Society of Nondestructive Testing, the term NDT includes many methods that can: (i) detect internal or external imperfections, (ii) determine structure, composition, or material properties, or (iii) measure geometric characteristics. Some typical structures or products inspected through the use of NDE technology are components of airplanes, motor vehicles, pipelines, bridges, trains, and power stations.

Nondestructive evaluation techniques can be broken down into seven main categories: (i) visual inspection, (ii) liquid penetration inspection, (iii) radiography and radiation testing, (iv) electromagnetic testing, (v) acoustic emission monitoring, (vi) magnetic methods, and (vii) ultrasonic testing. Each of these categories is broad, containing within them several specific testing techniques. The choice of an appropriate NDE technique depends on the specific application. We

will not go into detail on the benefits and limitations of each method, but will instead refer the reader to [8, 9, 18, 20, 38, 40] for a thorough discussion. In this paper, we will focus only on a particular electromagnetic testing method, called the eddy current method.

Eddy currents are currents found in any conducting material which is subjected to a time-varying magnetic field. They are useful for NDE purposes, because if a flaw is present within a conducting material, the flow of the eddy currents will be disrupted in some manner. From this disruption, and its effect on the magnetic flux density, one can often discern information about the damage or defect within the material. A thorough analysis of eddy currents and their behavior can be found in [44].

Since eddy currents are only found in a conducting material, the use of eddy current methods for interrogation is limited; however, these methods have been proven extremely useful when examining pipeline structures and aging aircrafts. There are many devices and eddy current techniques in use today including the self-nulling eddy current probe [49] along with conformal mapping techniques [50], the magneto-optic/eddy current imager [16, 45] in conjunction with eddy current imaging [17, 19], the SQUID (Superconducting Quantum Interference Device) through the use of either injected current methods or induced eddy current methods [11, 13, 22, 37, 39, 48] and the GMR (Giant Magnetoresistive) sensor based on the self-nulling probe design [51, 52]. Each of these instruments have unique features, making some instruments easier to use than others or more practical depending on the circumstances. Some of the instruments provide images of the damage, while others provide quantitative data. In this paper, we investigate computational methods for the estimation of a damage or flaw within a material using quantitative data taken by an appropriate instrument. In some cases, instruments providing images of the damage may give us valuable *a priori* information about the defect, allowing us to obtain a more accurate estimate of the damage.

Damage detection is quite naturally formulated in the context of inverse problems; in the case of electromagnetic probes these involve Maxwell's equations at some level. Consequently one can anticipate computational algorithms that are time and computer memory intensive. Motivated by goals of on-line, real-time algorithms to be used in portable testing devices, one is led to reduced order computational ideas. In an earlier paper [4] (see also [3]), we suggested techniques based on Proper Orthogonal Decomposition (also called Principal Component Analysis) methods and gave some initial computational results based on numerical simulations for one-dimensional damages which suggested significant potential for such an approach. In this paper we continue our investigations, providing theoretical foundations for the proposed approach along with a summary of extensive tests using numerical simulations for one-dimensional and two-dimensional damages. Moreover, we provide a summary of our efforts and results in using the reduced order algorithms with data from subsurface damage experiments designed and carried out specifically to test the efficacy of our proposed approach.

We first analyze a specific implementation of the eddy current method and develop a model describing the behavior of the magnetic flux density as a relationship to the total current. As a consequence, we will be able to obtain information about the damage from the relationship between the disruption in the eddy current and the resulting magnetic flux density.

2. Model Formulation

As discussed in the previous section, eddy currents are currents found in any conducting material subjected to some time-varying magnetic field and can be induced in a variety of ways. In this paper, we limit our discussion to only one implementation: we examine the process of inducing eddy currents within a sample by placing a thin conducting sheet carrying a uniform current above the sample. The current within the sheet produces a magnetic field perpendicular to it that in turn produces eddy currents within the sample. The presence of a flaw within the sample causes a disruption in the flow of the eddy currents and this disruption manifests itself in the magnetic flux density which can be measured by a device placed above the conducting sheet. A schematic of the inspection process is shown in Figure 1.

By assuming uniformity in the direction of the current flow in the conducting sheet (labeled the negative z direction, denoting the coordinate for the width of the sample in Figure 2), we are able to reduce the three-dimensional setup described above to a two-dimensional problem in the xy plane, where x denotes the coordinate of the length of the sample and y denotes the coordinate of the thickness of the sample. We make this simplifying assumption for proof-of-concept, to illustrate the feasibility of reconstructing the geometry of a damage. In addition, in order to disregard boundary effects along the edges of the sample, we assume the sample and conducting sheet are infinitely long, i.e., they are infinite in the x direction. If the conducting sheet and sample are not of infinite extent, we have to take into account the discontinuities in the current flow at the boundaries. Furthermore, the damage (which we shall refer to as a "crack") is assumed to be rectangular in shape and centered along the length of the sample (along the x direction) at $x = 0$.
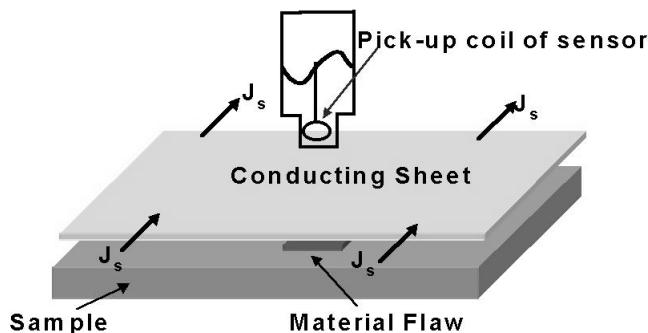

Figure 1. 3-D Schematic of Eddy Current Inspection Process

For computational purposes, we examine a finite "window" of the overall problem, which is called the computational domain Ω. In choosing the boundaries of the computational domain along the length of the sample (x boundaries), we recall that the sample and conducting sheet are assumed to be of infinite extent. Therefore, we can arbitrarily choose these boundaries by assigning evenly symmetric boundary conditions to account for the infinite extent of the materials. However, since the damage is centered along the length of the sample, we need to only consider half of the sample

for computational purposes. The other half will behave in the same manner. Therefore, we choose the left boundary to be located at the center of the crack in the x direction, labeled $x = 0$, with the crack symmetric through the yz plane at $x = 0$, and the right boundary is chosen at $x = 50mm$. The y boundaries, or top and bottom boundaries, are at $y = -35mm$ and $y = 35mm$ and are assumed to be far enough away from the sample that the field is approximately zero at these boundaries. Indeed, the magnetic flux density at a point is inversely proportional to the distance between the source current and that point. Hence the field tends to zero as the distance from the source current or conducting sheet increases. A schematic of the resulting two-dimensional problem is depicted in Figure 2 where it is assumed that the sample (which is $20mm$ thick) is composed of aluminum and the conducting sheet (which is $0.1mm$ thick) is made of copper. Thus the computational domain which we will use for the purposes of developing the model can be explicitly defined by

$$\Omega = \{(x, y, z) \in \mathbb{R}^3 : 0mm \leq x \leq 50mm, -35mm \leq y \leq 35mm\}.$$
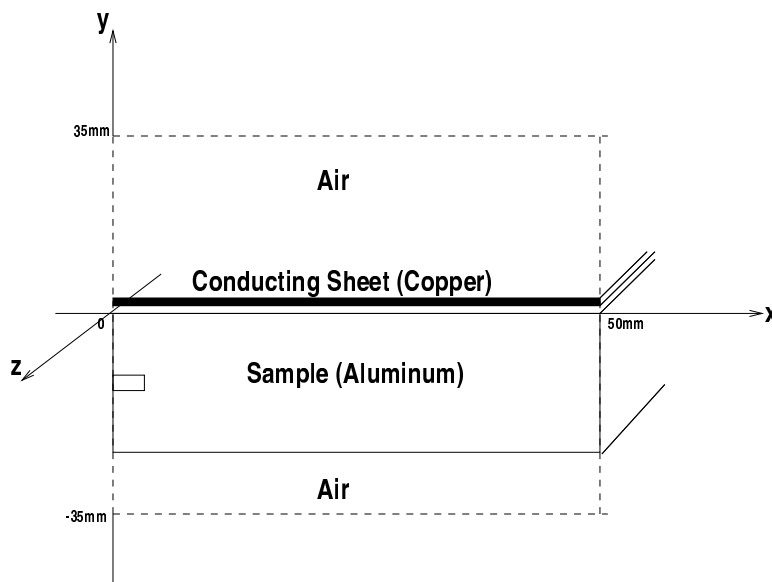
Figure 2. 2-D Schematic of Problem

We begin the development of the model by introducing a mathematical tool, called phasors, which is typically used in the field of electromagnetic nondestructive evaluation whenever periodic interrogating inputs are employed. As mentioned in the previous section, a conducting sheet (copper in our example) carrying a uniform current is placed above the sample to induce eddy currents within the sample. Without loss of generality, we assume the source current has the form

$$\tilde{\mathbf{J}}_s = J_s cos(\omega t)\hat{\mathbf{k}} = J_s Re(e^{i\omega t})\hat{\mathbf{k}}$$

where J_s is the magnitude of the source current. This current produces a magnetic field $\tilde{\mathbf{H}}(x, y, t)$ described by Maxwell's equations. As the magnetic field penetrates into the sample, a phase lag

occurs due to the finite conductivity of the sample (aluminum in our example). In other words, the magnetic field takes the form

$$\tilde{\tilde{\mathbf{H}}}(x, y, t) = \tilde{\mathbf{H}}(x, y)cos(\omega t + \theta(x, y)), \tag{1}$$

where $\tilde{\mathbf{H}}(x, y)$ is a vector field quantity which keeps track of the magnitude and direction of $\tilde{\tilde{\mathbf{H}}}$ at each point in space while $\theta(x, y)$ denotes the phase shift from the original cosine wave at the same point in space (this term takes into account the depth of penetration). Since these are the quantities of interest, we may use a vector phasor ([1, 10]), or a vector of complex numbers, $\mathbf{H}$ defined by

$$\tilde{\tilde{\mathbf{H}}}(x, y, t) = Re(\mathbf{H}(x, y)e^{i\omega t}) = Im(\mathbf{H}(x, y)e^{i(\omega t + \pi/2)}) \tag{2}$$

which keeps track of only these quantities.

We then use Maxwell's equations (they are the basis for all electromagnetic phenomena) in phasor form as the basis for our derivation. Details on the derivation of Maxwell equations in phasor form from Maxwell's equations as derived from first principles (e.g., Coulomb's law, the Lorentz transformation and relativity theory - see [14]), can be found in [23]. We then have for the basis of all the following derivations:

$$\nabla \cdot \mathbf{B} = 0, \tag{3}$$

$$\nabla \cdot \mathbf{D} = \rho, \tag{4}$$

$$\nabla \times \mathbf{E} = -i\omega\mathbf{B}, \tag{5}$$

and

$$\nabla \times \mathbf{H} = \mathbf{J} + i\omega\mathbf{D}. \tag{6}$$

We first make a couple of remarks regarding (3) - (6). To begin with, our system is considered to be electrically neutral, i.e., the internal electric charge density ρ equals zero. Secondly, by examining the conductivity, σ, of aluminum and copper ($\sigma_{al} = 3.72 \times 10^7 S/m$ and $\sigma_{cu} = 5.8 \times 10^7 S/m$ respectively) and by using Ohm's law

$$\mathbf{J} = \sigma\mathbf{E}, \tag{7}$$

we can argue $\mathbf{J} \approx 10^7\mathbf{E}$. On the other hand, the constitutive law

$$\mathbf{D} = \epsilon\mathbf{E}, \tag{8}$$

where ϵ is the electric permittivity ($\epsilon \approx \epsilon_0 \approx \frac{1}{36\pi} \times 10^{-7} F/m$), indicates $\mathbf{D} \approx 10^{-10}\mathbf{E}$. Therefore, for the source frequencies we consider within the scope of this paper ($f_s = 60$Hz - 2kHz), $\omega\mathbf{D} < 10^{-6}\mathbf{E}$ where $\omega = 2\pi f_s$ is the angular frequency. Consequently, in the sample and conducting sheet $\mathbf{J} >> \omega\mathbf{D}$ which implies we could assume $\omega\mathbf{D} \approx 0$ in both the sample and conducting sheet in (6). In other words, the term $\omega\mathbf{D}$ is only significant in the air. Both the literature and the finite element software employed in the computations (Ansoft Maxwell 2D Field Simulator) neglect the displacement current density in the air as well [28, 29, 30, 31, 47]. In our initial computational efforts, we formulated the problem both including as well as neglecting the displacement current density and compared the corresponding solutions. Our findings agreed with the literature; there was no

discernible change in the solution when the displacement current density was ignored. However, the presence of this term *does* alter the theoretical results slightly (see Section 3) and for this reason, we choose to include this term in the derivation of the model.

We use the Ansoft finite element solver ([1]) in our computational efforts; therefore, we continue our derivation in the same manner as done in Ansoft by introducing a magnetic vector potential $\mathbf{A}$. Based upon (3) and vector null identities, $\mathbf{B}$ can be represented as the curl of a vector potential $\mathbf{A}$ (called the magnetic vector potential),

$$\mathbf{B} = \nabla \times \mathbf{A}. \tag{9}$$

Therefore, given the magnetic vector potential $\mathbf{A}$, both the magnetic field $\mathbf{H}$ and magnetic flux density $\mathbf{B}$ can be computed. Accordingly, we want to combine Maxwell's equations to obtain equations in conjunction with boundary conditions which completely determine the behavior of the magnetic vector potential $\mathbf{A}$ in Ω.

Using the identity $\mathbf{B} = \nabla \times \mathbf{A}$ in (5), we have

$$\nabla \times \mathbf{E} = -i\omega(\nabla \times \mathbf{A}) \;\; \text{or} \;\; \nabla \times (\mathbf{E} + i\omega\mathbf{A}) = 0.$$

Again, using vector null identities, $\nabla \times (\mathbf{E} + i\omega\mathbf{A}) = 0$ implies $\mathbf{E} + i\omega\mathbf{A}$ can be written as the gradient of a scalar potential, denoted by ϕ. As a result,

$$\mathbf{E} = -i\omega\mathbf{A} - \nabla\phi. \tag{10}$$

Finally, we can use (6) and (10) in conjunction with Ohm's law (7), the constitutive law given by (8) and the constitutive law $\mathbf{H} = \frac{1}{\mu}\mathbf{B}$ (μ is the magnetic permeability in H/m), to obtain

$$\nabla \times \left(\frac{1}{\mu} \nabla \times \mathbf{A} \right) = (\sigma + i\omega\epsilon)(-i\omega\mathbf{A} - \nabla\phi) \quad \forall x, y \in \Omega. \tag{11}$$

In the above equality, the right side represents the total current density made up of the source current density, eddy current density, and displacement current density. The source current density $\mathbf{J}_s$ is due to differences in electric potential; therefore, $\mathbf{J}_s$ is represented by the term $-\sigma\nabla\phi$. The term $-i\omega\sigma\mathbf{A}$ represents the eddy current density $\mathbf{J}_e$ produced by a time-varying magnetic field. Finally, the displacement current density $\mathbf{J}_d$ due to time-varying electric fields is given by the term $i\omega\epsilon(-i\omega\mathbf{A} - \nabla\phi)$.

Since (11) contains two unknowns, $\mathbf{A}$ and ϕ, we need an additional equation to uniquely determine solutions of the system. In some instances, one is allowed to choose a "gauge" which often decouples the above equation; however, based upon the geometry in our test problem, $\nabla \cdot \mathbf{A} = 0$ is naturally imposed. This follows since the only nonzero component of $\mathbf{A}$ is A_3, the component of $\mathbf{A}$ in the z direction (the direction of the current density $\mathbf{J}$). Therefore, $\nabla \cdot \mathbf{A} = \frac{\partial A_3}{\partial z} = 0$ by uniformity in the z direction. Indeed, this is the Coulomb gauge [21, pp. 221-222].

Since the Coulomb gauge is naturally imposed, it provides no additional information in our problem. It is therefore necessary to use an integral constraint to obtain a second equation relating the magnetic vector potential $\mathbf{A}$ to the scalar potential ϕ, or more precisely $\nabla\phi$. For the integral constraint, we take the relationship

$$I = \int_S \mathbf{J}_t \cdot \mathbf{n}\,da = \int_S (\sigma + i\omega\epsilon)(-i\omega\mathbf{A} - \nabla\phi) \cdot \mathbf{n}\,da \tag{12}$$

where I is the total measurable current flowing in a conducting surface (S) and $\mathbf{J}_t$ is the total current density within the conducting surface. Since we are only able to control the current flowing in the conducting sheet, we use the equivalent equation in the conducting sheet

$$I_{cs} = \int_{cs} \mathbf{J}_t \cdot \mathbf{n}\,da = \int_{cs} (\sigma + i\omega\epsilon)(-i\omega\mathbf{A} - \nabla\phi) \cdot \mathbf{n}\,da \tag{13}$$

where I_{cs} is the total current flowing in the conducting sheet (cs). However, since (13) only provides a relationship between $\mathbf{A}$ and $\nabla\phi$ in the conducting sheet, we still need either a relationship between the potentials or a condition on one of the potentials in both the sample and air.

Using a few underlying assumptions, we can justify $\nabla\phi \equiv 0$ in the sample. We explore two different arguments which in the end result in this conclusion. One approach is to examine the source current density term caused by changes in potential across the material given by $\mathbf{J}_s = -\sigma\nabla\phi$. Since we only apply a current, and hence effectively a potential, across the conducting sheet, the source current density (due to changes in potential) only exists in the conducting sheet. Consequently, $\mathbf{J}_s = -\sigma\nabla\phi = 0$ in the sample. Since the conductivity of aluminum σ_{al} does not equal zero, $\nabla\phi$ must be identically zero for all points (x, y) in the sample. A second alternative is to assume the sample is a passive conductor modeling a short circuit (which is done in Ansoft). In general, a passive conductor is a conductor which has no component of source current (as discussed above). In other words, the only currents considered to be flowing in a passive conductor are eddy currents and displacement currents (when considered). In addition, a short circuit conductor is treated as a conducting ring which loops back on itself. In this case, using concepts of a closed circuit, the change in potential across the loop is zero [1, 46], i.e.,

$$\nabla\phi = 0 \quad \forall(x, y) \in sample. \tag{14}$$

The only other region left to consider is the air. When the displacement current density is ignored, it is not necessary to require an additional constraint on $\nabla\phi$ in the air since (11) reduces to

$$\nabla \times \left(\frac{1}{\mu}\nabla \times \mathbf{A}\right) = 0 \quad \forall(x, y) \in air. \tag{15}$$

However, we will make an intuitive argument for why $\nabla\phi$ should be taken to be zero in the air as well. We use an argument similar to that one used for the sample. The source current density, as discussed previously, is only present in the conducting sheet and hence not in the air. However, by examining the equations alone, this does not give us any knew information. It simply states that $J_s = -\sigma\nabla\phi$ must equal zero in the air which is already true since σ is identically zero in this region. On the other hand, we can intuitively argue that the source current density is due to changes in potential, and, therefore, if no source current density is present in a region, there should be no change in potential in that region as well. Using this reasoning, we take $\nabla\phi = 0$ in the air. Although not explicitly stated in the technical notes for Ansoft Maxwell 2D Field Simulator ([1]), the software effectively uses $\nabla\phi = 0$ in the air when estimating the displacement current density given the approximate finite element solution A determined by (13) and (14). (In the actual calculations produced by the Ansoft software, displacement current density is ignored totally.)

Therefore, combining all the above we have two coupled equations (11) and (13) and the additional condition $\nabla\phi = 0$ for points (x, y) in the sample and air. Using these equations, the magnetic vector potential **A** can be uniquely determined if appropriate boundary conditions on **A** are specified.

Recall that we assume evenly symmetric x boundaries due to the symmetry of the crack and the infinite extent of the materials. In other words on the x boundaries, we assume the fields on both sides of the boundary oscillate in the same direction. To account for the even symmetry, we assign Neumann boundary conditions to these boundaries. In a similar manner, we assume the y boundaries are "sufficiently far" away from the sample and scanning area to not effect the overall measurements. We mentioned previously that as one moves farther away from the sample and conducting sheet, the magnetic vector potential **A** tends to zero. Thus, on the y boundaries, we assign Dirichlet boundary conditions to indicate the boundary is "sufficiently far" away from the materials so that $\mathbf{A} \approx \mathbf{0}$. Therefore, the magnetic vector potential **A** is determined according to

$$\nabla \times \left(\frac{1}{\mu(x, y)} \nabla \times \mathbf{A}(x, y) \right) = (\sigma(x, y) + i\omega\epsilon(x, y))(-i\omega\mathbf{A}(x, y) - \nabla\phi) \quad x, y \in \Omega, \tag{16}$$

$$I_{cs} = \int_{cs} \mathbf{J}_t \cdot \mathbf{n}\, da = \int_{cs} (\sigma(x, y) + i\omega\epsilon(x, y))(-i\omega\mathbf{A}(x, y) - \nabla\phi) \cdot \mathbf{n}\, da \tag{17}$$

and

$$\nabla\phi = 0 \quad x, y \in \Omega \setminus cs \tag{18}$$

with

$$\begin{aligned}
\mathbf{A}(x, -35) &= 0 &= \mathbf{A}(x, 35) \\
\nabla\mathbf{A} \cdot \mathbf{n}|_{(0,y)} &= 0 &= \nabla\mathbf{A} \cdot \mathbf{n}|_{(50,y)}.
\end{aligned}$$

3. Well-Posedness

In the previous section we developed a model for the magnetic vector potential **A** given a source current I_{cs}. The boundary value problem is given in terms of two unknowns **A** and ϕ satisfying (16) and (17) with the additional condition given by (18) which, as we shall see, uniquely determines the solution when coupled with appropriate boundary conditions. However, we can reduce the above system into a single integro-differential equation by noting (see [23] for details) that the term $\nabla\phi$ is piecewise constant across all regions. Therefore, $\nabla\phi$ can be written in terms of **A** in (17). Hence we can combine all the equations as done in [23] to obtain the equivalent form of the boundary value problem

$$-\left(\frac{\partial^2 A(x, y)}{\partial x^2} + \frac{\partial^2 A(x, y)}{\partial y^2} \right) + \mu(x, y)(\sigma(x, y) + i\omega\epsilon(x, y))(i\omega A(x, y) + K(x, y)) = 0, \tag{19}$$

where $\nabla\phi = K(x, y)$ is defined by

$$K(x, y) = \begin{cases} -\frac{I_{cs}}{\Delta_{cs}(\sigma_{cu} + i\omega\epsilon_{cu})} - \frac{i\omega}{\Delta_{cs}} \int_{cs} A\, da & \text{for} \quad (x, y) \in cs \\ 0 & \text{for} \quad (x, y) \in \Omega \setminus cs \end{cases}. \tag{20}$$

Given this form of the equation, together with the boundary conditions, we consider the existence and uniqueness of a weak solution on a general domain given by

$$\tilde{\Omega} = \{(x, y, z) \in \mathbb{R}^3 : x_{min} \le x \le x_{max}, y_{min} \le y \le y_{max}\}$$

for which our test problem is a specific example. Then, let $H = L_2(\tilde{\Omega})$ and $V = \{\psi \in H^1(\tilde{\Omega}) | \psi(x, y_{min}) = 0 = \psi(x, y_{max})\}$ where we use the standard Sobolev space notation, $H^1(\tilde{\Omega}) = \{\psi \in L^2(\tilde{\Omega}) : \nabla\psi \in L^2(\tilde{\Omega})\}$. Note that we interpret pointwise evaluation of functions (along the boundary and elsewhere) in terms of a trace operator ([15]) for which we suppress notation throughout this paper . We denote by $\langle\phi, \psi\rangle \equiv \int_{\tilde{\Omega}} \phi\overline{\psi}da$ the standard inner product in H and $\langle\phi, \psi\rangle_V \equiv \int_{\tilde{\Omega}} \nabla\phi \cdot \overline{\nabla\psi}da$ the (H^1-equivalent) inner product in V.

Then using integration by parts together with natural boundary conditions and imposed conditions on test functions $\psi \in V$, the variational form of (19) is given by

$$\left(\langle\frac{\partial A}{\partial x}, \frac{\partial \psi}{\partial x}\rangle + \langle\frac{\partial A}{\partial y}, \frac{\partial \psi}{\partial y}\rangle\right) + \langle i\omega\mu(\sigma + i\omega\epsilon)A, \psi\rangle + \langle\mu(\sigma + i\omega\epsilon)K, \psi\rangle = 0 \tag{21}$$

or more precisely

$$\langle\nabla A, \nabla\psi\rangle + \langle\beta_1 A, \psi\rangle + \beta_2 \int_{cs} A\,da \int_{cs} \overline{\psi}\,da = \int_{cs} f\overline{\psi}\,da. \tag{22}$$

where $\beta_1 = i\omega\mu(\sigma + i\omega\epsilon)$, $\beta_2 = -\frac{i\omega\mu_{cu}(\sigma_{cu} + i\omega\epsilon_{cu})}{\Delta_{cs}}$, and $f = \frac{\mu_{cu}I_{cs}}{\Delta_{cs}}$.

3.1. Existence and Uniqueness

We consider the existence and uniqueness of the solution A to (22) (as well as to its equivalent formulation when the displacement current density is neglected) in the context of a Gelfand triple setting $V \hookrightarrow H \simeq H^* \hookrightarrow V^*$. We have that the embedding $V \hookrightarrow H$ is dense and continuous with

$$|\psi|_H \le k|\psi|_V \quad \text{for all } \psi \in V. \tag{23}$$

where the norm in V will be denoted by $|\cdot|_V$ and $|\cdot|$ will denote the norm in H for the rest of this section.

We define a sesquilinear form $\mathcal{L} : V \times V \to \mathbb{C}$ by

$$\mathcal{L}(\phi, \psi) = \langle\nabla\phi, \nabla\psi\rangle + \langle\beta_1\phi, \psi\rangle + \beta_2 \int_{cs} \phi\,da \int_{cs} \overline{\psi}\,da. \tag{24}$$

Then (22) can be written as

$$\mathcal{L}(A, \psi) = \int_{cs} f\overline{\psi}\,da. \tag{25}$$

We intend to prove $\mathcal{L}$ is V-continuous and for certain frequencies is V-elliptic. We will then invoke the Lax-Milgram theorem to prove the existence and uniqueness of the weak solution A to (22).

Lemma 3.1 $\mathcal{L}$ *is V-continuous, i.e., there exists some constant c_1 such that*

$$|\mathcal{L}(\phi, \psi)| \le c_1|\phi|_V|\psi|_V. \tag{26}$$

Proof: Using the triangle inequality, Cauchy-Schwartz inequality, properties of L^1, Holder's inequality and (23), we have

$$
\begin{aligned}
|\mathcal{L}(\phi, \psi)| &= |\langle \nabla\phi, \nabla\psi \rangle + \langle \beta_1\phi, \psi \rangle + \beta_2 \int_{cs} \phi da \int_{cs} \overline{\psi} da| \\
&\leq |\langle \phi, \psi \rangle_V| + |\langle \beta_1\phi, \psi \rangle| + |\beta_2 \int_{cs} \phi da \int_{cs} \overline{\psi} da| \\
&\leq |\phi|_V |\psi|_V + |\beta_1|_\infty |\phi||\psi| + |\beta_2| \int_{cs} |\phi| da \int_{cs} |\overline{\psi}| da \\
&\leq |\phi|_V |\psi|_V + |\beta_1|_\infty |\phi||\psi| + |\beta_2| |\phi|_{L^1(\Omega)} |\psi|_{L^1(\Omega)} \\
&\leq |\phi|_V |\psi|_V + |\beta_1|_\infty |\phi||\psi| + |1|^2 |\beta_2| |\phi||\psi| \\
&\leq (1 + k^2|\beta_1|_\infty + k^2|1|^2|\beta_2|)|\phi|_V |\psi|_V \\
&= c_1 |\phi|_V |\psi|_V,
\end{aligned}
$$

where $c_1 = 1 + k^2|\beta_1|_\infty + k^2|1|^2|\beta_2|$.

Lemma 3.2 *There exists $\mathcal{F} = \mathcal{F}(\mu, \epsilon, \tilde{\Omega})$ such that for $f_s < \mathcal{F}(\mu, \epsilon, \tilde{\Omega})$, there exists a constant $c_2 > 0$ such that $\mathcal{L}$ satisfies*

$$|\mathcal{L}(\phi, \phi)| \geq c_2 |\phi|_V^2. \tag{27}$$

Proof: By (24) and the definition of β_1 and β_2

$$
\begin{aligned}
Re\mathcal{L}(\phi, \phi) &= \langle \nabla\phi, \nabla\phi \rangle - \omega^2 \langle \mu\epsilon\phi, \phi \rangle + \frac{\omega^2 \mu_{cu}\epsilon_{cu}}{\Delta_{cs}} \int_{cs} \phi da \int_{cs} \overline{\phi} da \\
&= \langle \nabla\phi, \nabla\phi \rangle - \omega^2 \langle \mu\epsilon\phi, \phi \rangle + \frac{\omega^2 \mu_{cu}\epsilon_{cu}}{\Delta_{cs}} |\int_{cs} \phi da|^2.
\end{aligned}
$$

Therefore,

$$
\begin{aligned}
Re\mathcal{L}(\phi, \phi) &\geq \langle \nabla\phi, \nabla\phi \rangle - \omega^2 \langle \mu\epsilon\phi, \phi \rangle \\
&\geq \langle \nabla\phi, \nabla\phi \rangle - \omega^2 |\mu\epsilon|_\infty |\phi|^2.
\end{aligned}
$$

Denoting $a = max(|y_{min}|, |y_{max}|)$, we have $|y| \leq a$ for $(x, y) \in \tilde{\Omega}$. Hence for $\phi \in V$,

$$
\begin{aligned}
|\phi|^2 &= \int_{\tilde{\Omega}} 1 \cdot \phi\overline{\phi} da \\
&= \int_{x_{min}}^{x_{max}} \int_{y_{min}}^{y_{max}} 1 \cdot \phi\overline{\phi} dy dx \\
&= -\int_{\tilde{\Omega}} y \frac{\partial\phi}{\partial y}\overline{\phi} da - \int_{\tilde{\Omega}} y \frac{\partial\overline{\phi}}{\partial y}\phi da + \int_{x_{min}}^{x_{max}} y\phi\overline{\phi}|_{y_{min}}^{y_{max}} dx \\
&= -\langle y\frac{\partial\phi}{\partial y}, \phi \rangle - \langle y\phi, \frac{\partial\phi}{\partial y} \rangle \\
&\leq |\langle y\frac{\partial\phi}{\partial y}, \phi \rangle| + |\langle y\phi, \frac{\partial\phi}{\partial y} \rangle| \\
&\leq 2a|\phi||\nabla\phi| \\
&\leq \frac{2a}{4\gamma}|\phi|^2 + 2a\gamma|\nabla\phi|^2 \\
&= \frac{2a}{4\gamma}|\phi|^2 + 2a\gamma|\phi|_V^2.
\end{aligned}
$$

Thus,

$$\left(1 - \frac{2a}{4\gamma}\right)|\phi|^2 \leq 2a\gamma|\phi|_V^2$$

which gives us

$$|\phi|_V^2 - \left(1 - \frac{2a}{4\gamma}\right)|\phi|^2 \geq (1 - 2a\gamma)|\phi|_V^2.$$

We want to choose $0 < \gamma < \frac{1}{2a}$ such that

$$1 - \frac{2a}{4\gamma} = \omega^2 |\mu\epsilon|_\infty$$

or

$$\gamma = \frac{2a}{4(1 - \omega^2 |\mu\epsilon|_\infty)}.$$

Note that the condition $\gamma > 0$ is met if ω is chosen so that

$$\omega < \frac{1}{\sqrt{|\mu\epsilon|_\infty}}.$$

In order to satisfy the condition $\gamma < \frac{1}{2a}$, an initial source frequency must be chosen such that

$$\omega < \sqrt{\frac{1 - a^2}{|\mu\epsilon|_\infty}}$$

or

$$f_s < \frac{1}{2\pi} \sqrt{\frac{1 - a^2}{|\mu\epsilon|_\infty}}$$

where $\omega = 2\pi f_s$ and we tacitly assume $a^2 < 1$. Let $\mathcal{F} = \mathcal{F}(\mu, \epsilon, \tilde{\Omega}) = \frac{1}{2\pi}\sqrt{\frac{1-a^2}{|\mu\epsilon|_\infty}}$, then for $f_s < \mathcal{F}$,

$$Re\mathcal{L}(\phi, \phi) \geq |\phi|_V^2 - \omega^2 |\mu\epsilon|_\infty |\phi|^2 \geq c_2 |\phi|_V^2$$

with $c_2 = 1 - 2a\gamma > 0$.

We note that for our test problem, $\mu \approx \mu_0 = 4\pi \times 10^{-7}$, $\epsilon \approx \epsilon_0 \approx \frac{1}{36\pi} \times 10^{-7}$ and the term a discussed in the proof is given by $a = 3.5 \times 10^{-2}$. Hence, $\mathcal{F} \approx 4.77$ MHz. All of our computational results employ source frequencies $f_s < 2kHz$. Furthermore, frequencies much larger than these are not appropriate for this type of eddy current problem. We make one final remark about the bound $\mathcal{F}$ on source frequencies f_s. We note that $\mathcal{L}$ is of the form $\langle (B + kI)\phi, \psi \rangle_{V^*, V}$; therefore, a sharper bound on the source frequencies might be calculated by considering the spectrum of B and allowing those frequencies up to the point at which k becomes an eigenvalue of B. Since the bound $\mathcal{F}$ we have calculated is adequate for analysis including all calculations we consider in this paper, we do not choose to pursue this idea here.

A consequence of the Lax-Milgram theorem, as discussed in [53, pp. 271-275], gives an existence and uniqueness theorem for solutions:

Theorem 3.1 *Let $V \hookrightarrow H \hookrightarrow V^*$ be a Gelfand triple. Let $\mathcal{L} : V \times V \to \mathbb{C}$ satisfy:*

(A1) $|\mathcal{L}(\phi, \psi)| \leq c_1 |\phi|_V |\psi|_V$ for all $\phi, \psi \in V$,

(A2) $|\mathcal{L}(\phi, \phi)| \geq c_2 |\phi|_V^2$ for all $\phi \in V$.

Then there exists an operator $L : V \to V^*$ given by

$$\mathcal{L}(\phi, \psi) = \langle L\phi, \psi \rangle_{V^*, V}, \qquad \phi, \psi \in V \tag{28}$$

such that $L : V \to V^*$ is a linear topological isomorphism between the spaces V and V^*, and for the norms we have

$$|L| \leq c_1, \qquad |L^{-1}| \leq \frac{1}{c_2}. \tag{29}$$

Put otherwise, the weak equation

$$L\phi = f, \qquad f \in V^*, \tag{30}$$

interpreted as

$$\mathcal{L}(\phi, \psi) = \langle f, \psi \rangle \quad \text{for all } \psi \in V,$$

possesses for each $f \in V^*$ a unique solution $\phi \in V$, and this solution depends continuously on f.

Theorem 3.1 and Lemmas 3.1 and 3.2 readily give

Theorem 3.2 *There exists $\mathcal{F} = \mathcal{F}(\mu, \epsilon, \tilde{\Omega})$ such that for $f_s < \mathcal{F}(\mu, \epsilon, \tilde{\Omega})$, there exists a unique weak solution A to (22).*

We make a note that when the displacement current density is neglected, we obtain similar results to those above about *without* any restrictions on the source current density. In other words, given the variational form (found when ignoring the displacement current density)

$$\langle \nabla A, \nabla \psi \rangle + \langle \tilde{\beta}_1 A, \psi \rangle + \tilde{\beta}_2 \int_{cs} A\, da \int_{cs} \overline{\psi}\, da, = \int_{cs} f\overline{\psi}\, da \tag{31}$$

with coefficients $\tilde{\beta}_1 = i\omega\mu\sigma$ and $\tilde{\beta}_2 = -\frac{i\omega\mu_{cu}\sigma_{cu}}{\Delta_{cs}}$ we obtain the following theorem.

Theorem 3.3 *There exists a unique weak solution A to (31).*

3.2. Continuous Dependence on Parameters

In this section, we give theoretical results showing the solution A to (22) depends continuously on the parameters representing the damage which will also give us a basis for convergence results in the next section.

We begin by considering a general representation of a damage and define a parameter to represent this damage. Although we only consider rectangular damages centered along the length of the sample in our computational efforts, we will allow for any four sided polygon or quadrilateral in the theory. We will then relate our specific problem to the more general theory considered here.

Any quadrilateral can be represented by its four corners. Therefore, we let $\tilde{\mathbf{q}} \equiv [(x_1, y_1), (x_2, y_2), (x_3, y_3), (x_4, y_4)]$ be a vector in $\mathbb{R}^4 \times \mathbb{R}^2$ or equivalently $\mathbb{R}^8$ which represents the quadrilateral. We denote by $\tilde{Q}_{ad}$ the set of admissible parameters $\tilde{\mathbf{q}}$ where it is assumed $\tilde{Q}_{ad}$ is a compact subset of $\mathbb{R}^8$. We note that it is possible to pick $\tilde{Q}_{ad}$ to be compact since the damage is restricted to being within a sample of finite length and thickness. We also allow for the case in which no damage is present and represent this case by "collapsing" the quadrilateral into a single point (with zero area), i.e, we define $\tilde{\mathbf{q}}$ as a vector of identical points.

Then for any two damages given by parameters $\hat{\mathbf{q}}$ and $\tilde{\mathbf{q}}$ in $\tilde{Q}_{ad}$, let

$$\tilde{d}(\hat{\mathbf{q}}, \tilde{\mathbf{q}}) = ||\hat{\mathbf{q}} - \tilde{\mathbf{q}}|| = \left[(\hat{x}_1 - x_1)^2 + (\hat{y}_1 - y_1)^2 + ... + (\hat{x}_4 - x_4)^2 + (\hat{y}_4 - y_4)^2\right]^{1/2} \tag{32}$$

to be the standard Euclidean norm in $\mathbb{R}^8$. We denote by $\delta\hat{\Omega}$ (Figure 3) the points in Ω which are either in the damage represented by $\hat{\mathbf{q}}$ or $\tilde{\mathbf{q}}$ but which are not in both. In other words, let $\Omega_{\hat{\mathbf{q}}}$ represent the points (x, y) in Ω within the damage given by $\hat{\mathbf{q}}$ and $\Omega_{\tilde{\mathbf{q}}}$ the points (x, y) in Ω within the damage given by $\tilde{\mathbf{q}}$. Then $\delta\hat{\Omega} = \Omega_{\hat{\mathbf{q}}} \cup \Omega_{\tilde{\mathbf{q}}} - \Omega_{\hat{\mathbf{q}}} \cap \Omega_{\tilde{\mathbf{q}}}$. The area of $\delta\hat{\Omega}$ is directly related to the distance between parameters $\hat{\mathbf{q}}$ and $\tilde{\mathbf{q}}$. Indeed, $\tilde{d}(\hat{\mathbf{q}}, \tilde{\mathbf{q}}) \to 0$ if and only if $\tilde{x}_1 \to x_1$, $\tilde{y}_1 \to y_1$, ..., $\tilde{x}_4 \to x_4$, $\tilde{y}_4 \to y_4$, i.e., the four corners of the two damages approach one another. Therefore, $\tilde{d}(\hat{\mathbf{q}}, \tilde{\mathbf{q}}) \to 0$ implies $\delta\hat{\Omega} \to \emptyset$ and hence the area of $\delta\hat{\Omega} \to 0$.
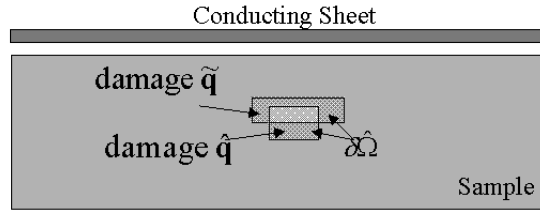
Figure 3. The Area Represented by $\delta\hat{\Omega}$

To relate this terminology to the computational examples we present in the rest of this paper, the only damages we consider computationally are those rectangular in shape and centered along the length of the axis. We only take into account half of the damage such that the left boundary of the portion we consider is located at $x = 0$ in the xy plane. Therefore, the only variation in the damage is in its length l, thickness h and depth d.

We let $\mathbf{q}$ be a parameter representing only these variations, i.e., $\mathbf{q}$ is a vector in some compact subset Q_{ad} of either $\mathbb{R}^1$, $\mathbb{R}^2$, or $\mathbb{R}^3$. For example, if we wish to only estimate the length of the damage, we assume the depth and thickness are fixed and hence $\mathbf{q} = q = l$ is in a compact subset of $\mathbb{R}^1$. However, if we wish to estimate parameters such as length and thickness while keeping the depth of the damage fixed, $\mathbf{q} = (l, h)$ and hence Q_{ad} is a subset of $\mathbb{R}^2$. If we allow all parameters to vary, $\mathbf{q} = (l, h, d) \in Q_{ad} \subset \mathbb{R}^3$. Therefore, given $\mathbf{q}$ (along with any fixed parameters) we have l, h, and d for which we can define $\tilde{\mathbf{q}} = [(0, -d), (l, -d), (l, -d - h), (0, -d - h)]$ to be the vector of corner points for the damage. This yields a formulation of the damage in terms of $\mathbf{q}$ that is equivalent to the formulation in terms of $\tilde{\mathbf{q}}$ given with metric $\tilde{d}$. Thus, if the solution depends continuously on $\tilde{\mathbf{q}}$, the solution will also depend continuously on the parameters we estimate given by $\mathbf{q}$.

Let $V(\delta\hat{\Omega}) = H^1(\delta\hat{\Omega})$ with the pseudo norm $|\phi|^2_{V(\delta\hat{\Omega})} = \int_{\delta\hat{\Omega}} \nabla\phi \nabla\overline{\phi} \, da$. Then given the terminology above, we first prove the sesquilinear form $\mathcal{L}$ depends continuously on $\tilde{\mathbf{q}}$ and use this result to obtain the continuous dependence of A on $\tilde{\mathbf{q}}$. We note that whether we include or neglect the displacement current density results in either frequency dependent or independent results, respectively. We only present the remaining theory with the displacement current density included.

Lemma 3.3 *There exists a positive constant K independent of the parameters $\hat{\mathbf{q}}, \tilde{\mathbf{q}}$ such that for all $\hat{\mathbf{q}}, \tilde{\mathbf{q}} \in \hat{Q}_{ad}$, the sesquilinear form $\mathcal{L}(\tilde{\mathbf{q}})(\cdot, \cdot)$ satisfies*

$$|\mathcal{L}(\tilde{\mathbf{q}})(\phi, \psi) - \mathcal{L}(\hat{\mathbf{q}})(\phi, \psi)| \le K|\phi|_{V(\delta\hat{\Omega})}|\psi|_V \tag{33}$$

for all $\phi, \psi \in V$ where $|\cdot|_{V(\delta\hat{\Omega})} \to 0$ when $\tilde{d}(\hat{\mathbf{q}}, \tilde{\mathbf{q}}) \to 0$.

Proof: By definition of the sesquilinear form $\mathcal{L}$ in (24)

$$|\mathcal{L}(\tilde{\mathbf{q}})(\phi, \psi) - \mathcal{L}(\hat{\mathbf{q}})(\phi, \psi)| = |\langle \nabla\phi, \nabla\psi \rangle + \langle \beta_1(\tilde{\mathbf{q}})\phi, \psi \rangle + \beta_2 \int_{cs} \phi \, da \int_{cs} \overline{\psi} \, da$$

$$-\langle \nabla\phi, \nabla\psi \rangle - \langle \beta_1(\hat{\mathbf{q}})\phi, \psi \rangle - \beta_2 \int_{cs} \phi \, da \int_{cs} \overline{\psi} \, da|$$

or simply

$$|\mathcal{L}(\tilde{\mathbf{q}})(\phi, \psi) - \mathcal{L}(\hat{\mathbf{q}})(\phi, \psi)| = |\langle (\beta_1(\tilde{\mathbf{q}}) - \beta_1(\hat{\mathbf{q}}))\phi, \psi \rangle|.$$

Using the definition of β_1, the Cauchy-Schwartz inequality and (23), we have

$$\begin{aligned}
|\langle (\beta_1(\tilde{\mathbf{q}}) - \beta_1(\hat{\mathbf{q}}))\phi, \psi \rangle| &\le |(\beta_1(\tilde{\mathbf{q}}) - \beta_1(\hat{\mathbf{q}}))\phi||\psi| \\
&\le |i\omega||(\mu(\tilde{\mathbf{q}})(\sigma(\tilde{\mathbf{q}}) + i\omega\epsilon(\tilde{\mathbf{q}})) - \mu(\hat{\mathbf{q}})(\sigma(\hat{\mathbf{q}}) + i\omega\epsilon(\hat{\mathbf{q}})))\phi||\psi| \\
&= \omega|\mu_{al}(\sigma_{al} + i\omega\epsilon_{al}) - i\omega\mu_0\epsilon_0||\phi|_{L^2(\delta\hat{\Omega})}|\psi| \\
&\le k^2\omega|\mu_{al}(\sigma_{al} + i\omega\epsilon_{al}) - i\omega\mu_0\epsilon_0||\phi|_{V(\delta\hat{\Omega})}|\psi|_V
\end{aligned}$$

where $\delta\hat{\Omega}$ is defined above. Therefore, if we let $K = k^2\omega|\mu_{al}(\sigma_{al} + i\omega\epsilon_{al}) - i\omega\mu_0\epsilon_0|$, we have

$$|\langle (\beta_1(\tilde{\mathbf{q}}) - \beta_1(\hat{\mathbf{q}}))\phi, \psi \rangle| \le K|\phi|_{V(\delta\hat{\Omega})}|\psi|_V. \tag{34}$$

Theorem 3.4 *Assume the admissible parameter set $\tilde{Q}_{ad}$ is a compact subset of $\mathbb{R}^8$. Then there exists $\mathcal{F} = \mathcal{F}(\mu, \epsilon, \tilde{\Omega})$ such that for source frequencies $f_s < \mathcal{F}(\mu, \epsilon, \tilde{\Omega})$, $\tilde{\mathbf{q}} \to A(\tilde{\mathbf{q}})$ is continuous from $\tilde{Q}_{ad}$ to V.*

Proof: Let $\tilde{\mathbf{q}}^n \to \tilde{\mathbf{q}} \in \tilde{Q}_{ad}$ and let $A(\tilde{\mathbf{q}}^n), A(\tilde{\mathbf{q}})$ be the corresponding solutions of (25). That is,

$$\mathcal{L}(\tilde{\mathbf{q}}^n)(A(\tilde{\mathbf{q}}^n), \psi) = \langle f, \psi \rangle \quad \text{for } \psi \in V \tag{35}$$

$$\mathcal{L}(\tilde{\mathbf{q}})(A(\tilde{\mathbf{q}}), \psi) \quad = \langle f, \psi \rangle \quad \text{for } \psi \in V. \tag{36}$$

Subtracting (36) from (35), we have

$$\mathcal{L}(\tilde{\mathbf{q}}^n)(A(\tilde{\mathbf{q}}^n), \psi) - \mathcal{L}(\tilde{\mathbf{q}})(A(\tilde{\mathbf{q}}), \psi) = 0.$$

Adding and subtracting the term $\mathcal{L}(\tilde{\mathbf{q}}^n)(A(\tilde{\mathbf{q}}), \psi)$ and simplifying, we have

$$\mathcal{L}(\tilde{\mathbf{q}}^n)(A(\tilde{\mathbf{q}}^n) - A(\tilde{\mathbf{q}}), \psi) = -[\mathcal{L}(\tilde{\mathbf{q}}^n) - \mathcal{L}(\tilde{\mathbf{q}})](A(\tilde{\mathbf{q}}), \psi).$$

Let $\psi = A(\tilde{\mathbf{q}}^n) - A(\tilde{\mathbf{q}})$. Then

$$\mathcal{L}(\tilde{\mathbf{q}}^n)(A(\tilde{\mathbf{q}}^n) - A(\tilde{\mathbf{q}}), A(\tilde{\mathbf{q}}^n) - A(\tilde{\mathbf{q}})) = -[\mathcal{L}(\tilde{\mathbf{q}}^n) - \mathcal{L}(\tilde{\mathbf{q}})](A(\tilde{\mathbf{q}}), A(\tilde{\mathbf{q}}^n) - A(\tilde{\mathbf{q}})).$$

Thus, using (33) we have

$$
\begin{aligned}
|\mathcal{L}(\tilde{\mathbf{q}}^n)(A(\tilde{\mathbf{q}}^n) - A(\tilde{\mathbf{q}}), A(\tilde{\mathbf{q}}^n) - A(\tilde{\mathbf{q}}))| &= |[\mathcal{L}(\tilde{\mathbf{q}}^n) - \mathcal{L}(\tilde{\mathbf{q}})](A(\tilde{\mathbf{q}}), A(\tilde{\mathbf{q}}^n) - A(\tilde{\mathbf{q}}))| \\
&\leq K|A(\tilde{\mathbf{q}})|_{V(\delta\Omega^n)}|A(\tilde{\mathbf{q}}^n) - A(\tilde{\mathbf{q}})|_V
\end{aligned}
$$

Then we can use the above equality and (27) where we note that c_2 can be established independent of $\mathbf{q}^n$ by following the proof of Lemma 3.2 in which $|\mu\epsilon|_\infty$ can be taken independent of q^n. Thus, defining $\tilde{K} = \frac{K}{c_2}$ independent of $\mathbf{q}^n$, we obtain

$$
|A(\tilde{\mathbf{q}}^n) - A(\tilde{\mathbf{q}})|_V \leq \tilde{K}|A(\tilde{\mathbf{q}})|_{V(\delta\Omega^n)}
$$

where the right side goes to 0 as $\tilde{\mathbf{q}}^n \to \tilde{\mathbf{q}}$.

3.3. Convergence Results

One possible estimation problem of interest consists of minimizing over some set Q_{ad} of admissible parameters the least squares functional

$$
J(\mathbf{q}) = \frac{1}{2} \sum_{i=1}^n \sum_{j=1}^m |A(x_i, y_j, \mathbf{q}) - \hat{A}^{ij}|^2 \tag{37}
$$

where $\{\hat{A}^{ij}\}$ are assumed to be some sampled data available at points $(x_i, y_j), i = 1, ..., n$, $j = 1, ..., m$. In practice, the computations for the minimizing problem are carried out using an approximate system. Here we will consider Galerkin type approximations in context of the variational formulation (22). Let H^N be a sequence of finite dimensional subspaces of H. We denote by P^N the orthogonal projection of H onto H^N. Then the parameter estimation problem can be formulated by seeking a $\mathbf{q} \in Q_{ad}$ which minimizes

$$
J^N(\mathbf{q}) = \frac{1}{2} \sum_{i=1}^n \sum_{j=1}^m |A^N(x_i, y_j, \mathbf{q}) - \hat{A}^{ij}|^2. \tag{38}
$$

The parameter estimation problem given above assumes we have sampled data $\hat{A}^{ij}$ along a grid of points (x_i, y_j), $i = 1, ..., n$, $j = 1, ..., m$ although it is not physically possible to obtain such data. Typically potentials, for example A, are only used for computational purposes. They allow one to overcome some of the difficulties which arise computationally when using field variables, the biggest complication being the number of equations which must be solved when using field variables [30]. The field $\mathbf{B}$ or $\mathbf{H}$, however, is the only measurable quantity.

Therefore we also explore an alternative problem which we use in much of our computational and experimental investigations. It involves cost functionals using observations of the magnetic flux density $\mathbf{B} = \nabla \times \mathbf{A} = (\frac{\partial A}{\partial y}, -\frac{\partial A}{\partial x}, 0) = (B_1, B_2, 0)$. In this case, (37) and (38) are replaced by

$$
J(\mathbf{q}) = \frac{1}{2} \sum_{i=1}^n \sum_{j=1}^m |B_k(x_i, y_j, \mathbf{q}) - \hat{B}_k^{ij}|^2 \tag{39}
$$

and

$$
J^N(\mathbf{q}) = \frac{1}{2} \sum_{i=1}^n \sum_{j=1}^m |B_k^N(x_i, y_j, \mathbf{q}) - \hat{B}_k^{ij}|^2 \tag{40}
$$

respectively, for $k = 1$ or 2.

However, in actual experimental situations, the sensor detects magnetic flux density across the entire surface area of the sensor and then outputs this data as data for a specific point. This necessarily involves averaging of the data over the area in some fashion. Therefore we can assume

$$\hat{B}_k^{ij} \approx \frac{1}{|\tilde{\Omega}_{ij}|} \int_{\tilde{\Omega}_{ij}} B(x, y; \mathbf{q}^*) da \tag{41}$$

where $\mathbf{q}^*$ represents exact parameter values corresponding to the damage within the sample from which the data was obtained and $\tilde{\Omega}_{ij}$ is a neighborhood of (x_i, y_j). Hence we instead consider cost functionals of the form

$$J(\mathbf{q}) = \frac{1}{2} \sum_{i=1}^{n} \sum_{j=1}^{m} |\mathcal{C}^{ij} B_k(\mathbf{q}) - \hat{B}_k^{ij}|^2 \tag{42}$$

and

$$J^N(\mathbf{q}) = \frac{1}{2} \sum_{i=1}^{n} \sum_{j=1}^{m} |\mathcal{C}^{ij} B_k^N(\mathbf{q}) - \hat{B}_k^{ij}|^2 \tag{43}$$

as well as the corresponding cost functionals in terms of A where

$$\mathcal{C}^{ij} B_k(\mathbf{q}) = \frac{1}{|\tilde{\Omega}_{ij}|} \int_{\tilde{\Omega}_{ij}} B_k(x, y; \mathbf{q}) da.$$

Thus, using the notation and results developed in this section, we obtain the following result.

Theorem 3.5 *Suppose*

(B1) The finite dimensional subspaces H^N satisfy $H^N \subset V$.

(B2) For each $\psi \in V, |P^N \psi - \psi|_V \to 0$ as $N \to \infty$.

Let $\tilde{\mathbf{q}}^N$ be arbitrary in $\tilde{Q}_{ad}$ such that $\tilde{\mathbf{q}}^N \to \tilde{\mathbf{q}}$ in $\tilde{Q}_{ad}$. Then there exists $\mathcal{F} = \mathcal{F}(\mu, \epsilon, \tilde{\Omega})$ such that for source frequencies $f_s < \mathcal{F}(\mu, \epsilon, \tilde{\Omega})$, we have $A^N(\tilde{\mathbf{q}}^N) \to A(\tilde{\mathbf{q}}) \in V$ as $N \to \infty$, where $A(\tilde{\mathbf{q}})$ is the solution to (25).

Proof: We have

$$\mathcal{L}(\tilde{\mathbf{q}}^N)(A^N(\tilde{\mathbf{q}}^N), \psi^N) = \langle f, \psi^N \rangle \quad \text{for } \psi^N \in H^N \tag{44}$$
$$\mathcal{L}(\tilde{\mathbf{q}})(A(\tilde{\mathbf{q}}), \psi) = \langle f, \psi \rangle \quad \text{for } \psi \in V. \tag{45}$$

We also can write

$$|A^N(\tilde{\mathbf{q}}^N) - A(\tilde{\mathbf{q}})|_V \leq |A^N(\tilde{\mathbf{q}}^N) - P^N A(\tilde{\mathbf{q}})|_V + |P^N A(\tilde{\mathbf{q}}) - A(\tilde{\mathbf{q}})|_V.$$

Hence from (B2) it suffices to prove

$$|A^N(\tilde{\mathbf{q}}^N) - P^N A(\tilde{\mathbf{q}})|_V \to 0 \quad \text{for } \tilde{\mathbf{q}}^N \to \tilde{\mathbf{q}} \in \tilde{Q}_{ad} \quad \text{as } N \to \infty.$$

Taking $\psi = \psi^N$ in (45) and subtracting from (44), we obtain

$$\mathcal{L}(\tilde{\mathbf{q}}^N)(A^N(\tilde{\mathbf{q}}^N), \psi^N) - \mathcal{L}(\tilde{\mathbf{q}})(A(\tilde{\mathbf{q}}), \psi^N) = 0$$

for $\psi^N \in H^N$. Furthermore, by adding and subtracting $\mathcal{L}(\tilde{\mathbf{q}}^N)(P^N A(\tilde{\mathbf{q}}), \psi^N)$ and $\mathcal{L}(\tilde{\mathbf{q}}^N)(A(\tilde{\mathbf{q}}), \psi^N)$ and simplifying, we have

$$\mathcal{L}(\tilde{\mathbf{q}}^N)(A^N(\tilde{\mathbf{q}}^N) - P^N A(\tilde{\mathbf{q}}), \psi^N) + \mathcal{L}(\tilde{\mathbf{q}}^N)(P^N A(\tilde{\mathbf{q}}) - A(\tilde{\mathbf{q}}), \psi^N)$$
$$+ [\mathcal{L}(\tilde{\mathbf{q}}^N) - \mathcal{L}(\tilde{\mathbf{q}})](A(\tilde{\mathbf{q}}), \psi^N) = 0.$$

Choosing $\psi^N = \Delta^N = A^N(\tilde{\mathbf{q}}^N) - P^N A(\tilde{\mathbf{q}})$, we find that

$$\mathcal{L}(\tilde{\mathbf{q}}^N)(\Delta^N, \Delta^N) + \mathcal{L}(\tilde{\mathbf{q}}^N)(P^N A(\tilde{\mathbf{q}}) - A(\tilde{\mathbf{q}}), \Delta^N) + [\mathcal{L}(\tilde{\mathbf{q}}^N) - \mathcal{L}(\tilde{\mathbf{q}})](A(\tilde{\mathbf{q}}), \Delta^N) = 0.$$

Therefore,

$$|\mathcal{L}(\tilde{\mathbf{q}}^N)(\Delta^N, \Delta^N)| = |-\mathcal{L}(\tilde{\mathbf{q}}^N)(P^N A(\tilde{\mathbf{q}}) - A(\tilde{\mathbf{q}}), \Delta^N) - [\mathcal{L}(\tilde{\mathbf{q}}^N) - \mathcal{L}(\tilde{\mathbf{q}})](A(\tilde{\mathbf{q}}), \Delta^N)|.$$

However, using the triangle inequality, (26), (33), and the Cauchy-Schwartz inequality, we can bound the right side of the above by

$$|-\mathcal{L}(\tilde{\mathbf{q}}^N)(P^N A(\tilde{\mathbf{q}}) - A(\tilde{\mathbf{q}}), \Delta^N) - [\mathcal{L}(\tilde{\mathbf{q}}^N) - \mathcal{L}(\tilde{\mathbf{q}})](A(\tilde{\mathbf{q}}), \Delta^N)| \leq$$
$$(c_1 |P^N A(\tilde{\mathbf{q}}) - A(\tilde{\mathbf{q}})|_V + K|A(\tilde{\mathbf{q}})|_{V(\delta\Omega^N)})|\Delta^N|_V$$

where c_1 is the constant in Lemma 3.1 and K is the constant in Lemma 3.3. We can conclude using (27) that

$$|\Delta^N|_V \leq \frac{c_1}{c_2}|P^N A(\tilde{\mathbf{q}}) - A(\tilde{\mathbf{q}})|_V + \frac{K}{c_2}|A(\tilde{\mathbf{q}})|_{V(\delta\Omega^N)}|A(\tilde{\mathbf{q}})|_V.$$

Thus, given any $\tilde{\mathbf{q}}^N \to \tilde{\mathbf{q}} \in \tilde{Q}_{ad}$, it follows from (B2) that $\Delta^N = A^N(\tilde{\mathbf{q}}^N) - P^N A(\tilde{\mathbf{q}}) \to 0$ as $N \to \infty$, giving us the desired results.

We note that the results above guarantee convergence of both $A^N(\mathbf{q})$ to $A(\mathbf{q})$ in V and $\mathbf{B}^N(\mathbf{q}) \to \mathbf{B}(\mathbf{q})$ in $L^2(\tilde{\Omega})$ and hence provides a complete theory for the inverse problem considered (see the general framework given in Chapter 5 of [5]).

4. Computational Method

Our ultimate goal is to determine the feasibility of using a portable sensing device in conjunction with inverse problem techniques to characterize the geometry of a hidden, i.e., subsurface, damage within a sample. To achieve this goal, we must develop fast and efficient forward computational methods to be used possibly numerous times in the inverse problem formulated in the next two sections. To this end, we examine reduced order Karhunen-Loeve or Proper Orthogonal Decomposition (POD) techniques.

The POD technique is an attractive order reduction method, because basis elements are formed in an "optimal" way which span a data set consisting of either numerical simulations or experimental data. Since the POD basis is formed so that *each* basis element captures important aspects of the data set, only a small number of POD basis elements are needed in general to describe the solution [36]. Consequently, if the POD method is successful, implementation should result in a decrease of computational time.

We summarize the use of the POD method in the context of the least squares inverse problems described in detail in Sections 5 and 6 and first introduced in [3, 4] for these problems. For further details on the general POD method, we refer the reader to [2, 6, 7, 12, 24, 26, 27, 32, 33, 34, 35, 36] and the extensive list of references contained therein.

The first step in forming the POD basis is to collect "snapshots" or solutions across time, space or a varied parameter. In our case, we let $\mathbf{q}$ be the vector parameter characterizing physical properties of the damage; i.e., as discussed in Section 3.2, $\mathbf{q}$ determines the geometry of the damage including the length, thickness, depth, etc. of the damage. For an ensemble of damages $\{\mathbf{q}_j\}_{j=1}^{N_s}$, we obtain corresponding solutions, $\{\mathbf{A}(\mathbf{q}_j)\}_{j=1}^{N_s}$, of (16) with (17) and (18), for magnetic vector potentials which we call our "snapshots". Alternatively, from the solution set $\{\mathbf{A}(\mathbf{q}_j)\}_{j=1}^{N_s}$, we can obtain the magnetic fluxes $\{\mathbf{B}(\mathbf{q}_j)\}_{j=1}^{N_s}$ and instead use these as our "snapshots" if we wish to treat magnetic fluxes as our basic state variable. (In [3] we compare results using one field versus the other as the basic state variable. The conclusions are summarized in Section 5.) For our explanation, we will consider snapshots on $\mathbf{A} = (0, 0, A_3)$ and hence our explanation will be for the scalar case. For the vector case, we would simply proceed componentwise [2, 12, 36]. Without loss of generality, we will denote the vector $\mathbf{A}$ by its scalar nonzero component A, i.e., the A_3 component of $\mathbf{A}$.

We seek basis elements of the form

$$\Phi_i = \sum_{j=1}^{N_s} V_i(j) A(\mathbf{q}_j) \tag{46}$$

where the coefficients $V_i(j)$ are chosen such that each POD basis element Φ_i, $i = 1, 2, ..., N_s$, maximizes

$$\frac{1}{N_s} \sum_{j=1}^{N_s} |\langle A(\mathbf{q}_j), \Phi_i \rangle_{L^2(\Omega, \mathbb{C})}|^2$$

subject to $\langle \Phi_i, \Phi_i \rangle_{L^2(\Omega, \mathbb{C})} = ||\Phi_i||^2 = 1$. Standard arguments guarantee that the coefficients $V_i(j)$ can be found by solving the eigenvalue problem

$$CV = \lambda V$$

where the "covariance" matrix C is defined by

$$[C]_{ij} = \frac{1}{N_s} \langle A(\mathbf{q}_i), A(\mathbf{q}_j) \rangle_{L^2(\Omega, \mathbb{C})}.$$

The matrix C is a Hermitian positive semi-definite matrix, and thus it possesses a complete set of orthogonal eigenvectors with corresponding nonnegative real eigenvalues. We order the eigenvalues along with their corresponding eigenvectors such that the eigenvalues are in decreasing order,

$$\lambda_1 \geq \lambda_2 \geq ... \geq \lambda_{N_s} \geq 0.$$

We furthermore normalize the eigenvectors corresponding to the rule

$$V_i \cdot V_j = \frac{\delta_{ij}}{N_s \lambda_j}.$$

Then the ith POD basis element is defined by (46) where $V_i(j)$ represents the jth component of the ith eigenvector of C. It can also be shown that $\{\Phi_i\}_{i=1}^{N_s}$ are orthonormal in $L^2(\Omega, \mathbb{C})$ and $span\{\Phi_i\}_{i=1}^{N_s} = span\{A(\mathbf{q}_j)\}_{j=1}^{N_s}$. Indeed, given any $A(\mathbf{q}_j)$, we have

$$A(\mathbf{q}_j) = \sum_{k=1}^{N_s} \alpha_k(\mathbf{q}_j)\Phi_k$$

where

$$\alpha_k(\mathbf{q}_j) = \langle A(\mathbf{q}_j), \Phi_k \rangle_{L^2(\Omega,\mathbb{C})}.$$

We point out that if any of the λ_i's are zero, say $\lambda_i = 0$ for $i = K + 1, ..., N_s$, then even though the corresponding V_i are orthogonal (and of course linearly independent), we will have $span\{\Phi_i\}_{i=1}^{K} = span\{\Phi_i\}_{i=1}^{N_s}$. In this case we will only generate $K < N_s$ linearly independent POD basis elements. A discussion of the relation between POD basis element formation and the popular singular value decomposition (SVD) methods in linear algebraic methods is given in [32].

To determine the reduced number N of POD basis elements required to accurately portray the ensemble of "snapshots" $\{A(\mathbf{q}_j)\}_{j=1}^{N_s}$, we consider

$$\sum_{j=1}^{N} \lambda_j / \sum_{j=1}^{N_s} \lambda_j \tag{47}$$

which represents the percentage of "energy" in $span\{A(\mathbf{q}_j)\}_{j=1}^{N_s}$ that is captured in $span\{\Phi_j\}_{j=1}^{N}$. The reduced basis consists of only the first N elements Φ_i, $i = 1, ..., N$, where N is chosen according to the percentage "energy" desired. We intuitively argue that the "energy" we are referring to is related to the total electrostatic energy. Simply stated, the matrix C contains terms of the form

$$\int_\Omega A\overline{A}da = \int_\Omega |A|^2 da.$$

which can be written in terms of the electric field E according to (10), $E = -i\omega A - \nabla\phi$. Therefore,

$$\int_\Omega |A|^2 da = C_1 \int_\Omega |E + \nabla\phi|^2 da.$$

where $C_1 = \frac{1}{\omega^2}$. Since $\nabla\phi$ is piecewise constant (proved in [23]), the terms in the matrix C are a perturbation of terms associated with electrostatic energy given by

$$W_E = \frac{1}{2}\epsilon_0 \int_V |E|^2 dV.$$

Thus we conclude that when we snapshot on the magnetic vector potential, the ratio in (47) is a measure of the electrostatic energy stored across Ω (see [14]).

Employing only the first N POD basis elements, we obtain the approximation $A^N(\mathbf{q}_j)$ for $A(\mathbf{q}_j)$ such that

$$A(\mathbf{q}_j) \approx A^N(\mathbf{q}_j) \equiv \sum_{k=1}^{N} \alpha_k(\mathbf{q}_j)\Phi_k.$$

To approximate $A^N(\mathbf{q})$ where $\mathbf{q}$ is a given parameter *not* in the set $\{\mathbf{q}_j\}_{j=1}^{N_s}$, we must extend the approximation formula to obtain

$$A^N(\mathbf{q}) = \sum_{k=1}^{N} \alpha_k(\mathbf{q})\Phi_k. \tag{48}$$

Two possible ways of computing $\alpha_k(\mathbf{q})$ are by using a POD/Galerkin method or a POD/Interpolation method. The traditional way to find $\alpha_k(\mathbf{q})$ is to use a POD/Galerkin method; however, there are many advantages in choosing a POD/Interpolation method. We next examine both methods and compare the advantages and disadvantages of each.

The first approach we consider, the POD/Galerkin approach is essentially an application of Galerkin's method to the integro-differential equation (19) in conjunction with the reduced order POD method. The POD/Galerkin method uses the approximation given in (48) in the variational form of the integro-differential equation where the test functions are chosen to be the reduced order POD basis elements $\{\Phi_i\}_{i=1}^{N}$. The system then reduces to a linear system which we can solve for the coefficients $\alpha_k(\mathbf{q})$, $k = 1, ..., N$.

In our computational efforts reported on here we follow the literature ([28, 29, 30, 31, 47]) and neglect the displacement current in the numerical implementation. Therefore, we will use the variational form

$$\left(\langle \frac{1}{\mu}\frac{\partial A}{\partial x}, \frac{\partial \psi}{\partial x} \rangle + \langle \frac{1}{\mu}\frac{\partial A}{\partial y}, \frac{\partial \psi}{\partial y} \rangle \right) + \langle i\omega\sigma A, \psi \rangle - \frac{i\omega\sigma_{cu}}{\Delta_{cs}} \int_{cs} A\, da \int_{cs} \overline{\psi}\, da = \frac{I_{cs}}{\Delta_{cs}} \int_{cs} \overline{\psi}\, da. \tag{49}$$

Substituting (48) into (49) and letting $\psi = \Phi_l$, $l = 1, ..., N$, we obtain the system

$$\left(K + i\omega M - \frac{i\omega\sigma_{cu}}{\Delta_{cs}} b\overline{b}^T \right) \alpha = \frac{I_{cs}}{\Delta_{cs}} b \tag{50}$$

for $\alpha = [\alpha_1, \alpha_2, ..., \alpha_N]^T$ where

$$[K]_{lk} = \left(\int_{\Omega} \frac{1}{\mu} \left(\frac{\partial \Phi_k}{\partial x}\frac{\overline{\partial \Phi_l}}{\partial x} + \frac{\partial \Phi_k}{\partial y}\frac{\overline{\partial \Phi_l}}{\partial y} \right) da \right),$$

$$[M]_{lk} = \int_{\Omega} \sigma \Phi_k \overline{\Phi_l}\, da,$$

and

$$[b]_l = \int_{cs} \overline{\Phi_l}\, da.$$

Recall $\mu \approx \mu_0$ and therefore, changes in the parameter vector $\mathbf{q}$ only change the conductivity σ and therefore only effects the matrix M. Consequently, in the inverse problem, for each "new guess" of $\mathbf{q}$, only the matrix M must be recalculated with each iterative step. This reduces the time required for each forward estimation and hence the total time for the entire inverse problem.

Another approach to forming the POD approximation is to use POD/Interpolation to calculate the coefficients. This method relies entirely on the values of the coefficients $\alpha_k(\mathbf{q})$ for $\mathbf{q}$ in the set $\{\mathbf{q}_j\}_{j=1}^{N_s}$. Unlike the POD/Galerkin method, it does not take into account the boundary value problem which A satisfies.

Various interpolation methods may be chosen to evaluate $\alpha_k(\mathbf{q})$ such as linear interpolation, cubic spline interpolation or nearest neighbor interpolation. However, in the simulations presented here, the built-in Matlab interpolation functions *interp1* or *interp2*, one-dimensional interpolation and two-dimensional interpolation respectively, were used. The linear interpolation method was chosen for the one-parameter simulated case and cubic spline interpolation was chosen for all other estimation problems. We chose these methods because initial trials suggested this would be the best method to choose in order to achieve the most accurate results in the inverse problem. For a more detailed discussion on these interpolation techniques, we will refer the reader to [42, pp. 348-353] and [43, pp. 93-106].

A detailed discussion, including graphical illustrations, of the accuracy of the POD approximations compared to Ansoft finite element approximations using each method can be found in [23] when approximating one parameter (length of damage). Here we summarize those results. When applying the POD/Galerkin method, using only $N = 3$ POD basis elements, we were able to fairly accurately approximate the finite element solution which uses over 7000 finite elements in its approximation. However, as the value of N increases, the approximation continually worsens as the conditioning of the linear system being solved deteriorates. When $N = 3$ basis elements are used, the condition number is approximately 80; however, the condition number jumps to approximately 360 when using $N = 4$ elements. Moreover, the condition number is over 12,000 when all of the POD basis elements ($N = 21$) are used in the approximation. The relative error in the approximation also indicates that the best approximation is found when $N = 3$ and continually worsens for larger values of N; therefore, the optimal value of N to use in this optimization problem appears to be $N = 3$.

The POD/Interpolation method does a considerably better job at approximating the finite element solution with only 2-3 basis elements. With $N = 2$ basis elements, there is still some visible error in the approximation, but the approximation and finite element simulation are approximately the same, with less than a 1% relative error.

From the examples described above, there are cases in which the POD/Interpolation method clearly produces more accurate results. We cannot make this generalization in all cases; nonetheless, one distinct advantage of the POD/Interpolation method is that *it does not rely on the equations describing the system.* This can be very useful in some experimental applications in which data is available but it is not easy to precisely model the physical process corresponding to the data. In this case, if there is correlation in the data, the POD method may be a viable approximation method in which an appropriate option for determining the coefficients would be a POD/Interpolation method.

5. Simulated Results

In this section we present computational results for the least squares inverse problem based on the methodology developed in Section 4. We are concerned with identifying the geometry of a crack, i.e., estimating parameters such as the length, thickness, and depth of a crack within a sample. To determine the feasibility of this task and to illustrate the use of the reduced order methodology, we first estimate a single parameter keeping the other two parameters fixed. We

estimate length, thickness and depth separately, and then carry out a two-dimensional parameter estimation, estimating both length and depth simultaneously.

In [3] and [4], we performed several trials in which we assumed we had access to various types of data, such as the A field or the $\mathbf{B}$ field at various points (x_i, y_j) in Ω. We compared and contrasted the accuracy to which we could estimate the length l of the damage based on whether the A field or $\mathbf{B}$ field was used and whether we considered the field along a single line, multiple lines or within the entire region (which is not physically possible and was only tested for hypothetical comparisons). From the results in these references, we concluded that extremely accurate results were obtained *only* when the y component B_2 of the magnetic flux density was used in the cost criterion, i.e., when we used

$$J(\mathbf{q}) = \frac{1}{2} \sum_{i=1}^{n} \sum_{j=1}^{m} |10^8 B_2^N(x_i, y_j, \mathbf{q}) - 10^8 \hat{B}_2^{ij}(\mathbf{q}^*)|^2 \tag{51}$$

where 10^8 is a scaling factor accounting for the low order of magnitude of the field (B_2 is on the order of $10^{-8} Wb/m$), $B_2^N(\mathbf{q})$ is the reduced order POD approximation to the magnetic flux density given by $B^N = \nabla \times A^N$, and $\hat{B}$ is "data" from a sample we wish to characterize. (In this section, $\hat{B}$ is obtained from finite element simulations with $\mathbf{q} = \mathbf{q}^*$ to which randomly generated noise has been added in the usual manner (see [4] or [23]). Furthermore, performing multi-line scans or using full region data improved the results only marginally and hence did not warrant the extra effort and time in collecting more extensive data sets. Consequently the results presented in this section involve only the least squares difference in the B_2 field given by (51) along a single line located $1mm$ above the conducting sheet.

We discussed above two different methods used in forming the reduced order POD approximation: the POD/Galerkin method and POD/Interpolation method. As mentioned previously the POD/Interpolation method did much better at approximating the finite element solution; therefore, we only present here the inverse problem results obtained using that method. We refer the interested reader to [23] for a summary of and comparison with results using the POD/Galerkin method.

5.1. Estimating One Parameter

In the one-parameter estimation problem, we estimated three different lengths ($l^* = 1.3mm$, $l^* = 2.5mm$ and $l^* = 5mm$), one thickness ($h^* = 1.3mm$) and three different depths ($d^* = 3mm$, $d^* = 8mm$ and $d^* = 11mm$) while keeping all other parameters fixed. In estimating the length of the damage, we generated an ensemble of damages keeping the thickness fixed at $2mm$ with various crack lengths $\{l_j\}_{j=1}^{N_s}$ at a fixed depth of $9mm$. We varied the lengths from $0mm$ to $4mm$ in increments of $0.2mm$ resulting in $N_s = 21$ different damages and use the commercial software Ansoft Maxwell 2D Field Simulator to generate snapshots $\{A(l_j)\}_{j=1}^{N_s}$. Similarly, in estimating the thickness of the damage, we kept the length fixed at $2mm$ and depth fixed at $9mm$ and varied the thickness from $0mm$ to $4mm$ in increments of $0.2mm$. Finally, in estimating the depth, we kept the length of the damage fixed at $1.5mm$ and thickness fixed at $0.5mm$. We took snapshots on A

for damages with depths ranging from $0.25mm$ to $19.25mm$ in increments of $0.5mm$ ($N_s = 39$ total snapshots). Since we added random error to the data to mimic normal random measurement error found in experimental data, we generated ten different sets of random error which was added to the data and averaged the results across the ten trials to obtain an average result along with a standard deviation across the ten trials. (See [23] for full details.) Using the optimization Nelder-Mead ([25, 41]), we obtained the results in Table 1.

Table 1. Results Estimating a Single Parameter Keeping All Other Parameters Fixed at a 10% Relative Noise Level

q (in mm)	No. POD	True $\mathbf{q}^*$ in data	Avg. Est. **q**	St. Dev.
length	4	1.3	1.2977	0.0057
	4	2.5	2.4981	0.0020
	4	5.0	4.9771	0.0066
thickness	9	1.3	1.3056	0.0054
depth	5	3.0	3.0349	0.0115
	5	8.0	8.0631	0.0109
	5	11.0	10.9184	0.0107

We note that in each case, we considered parameters *not* included in those upon which we snapshot. Furthermore, we consider one case in which the parameter value was outside the interval upon which we took snapshots. In other words, when estimating length $l^* = 5mm$, the POD/Interpolation method could not be used. We instead considered POD/Extrapolation. Nonetheless in all the results presented, the method was shown to be quite accurate with low standard deviations in all cases. We also note that although we have reported on three estimated depths in which we obtained extremely accurate estimates, in some of the cases tested, the results were not quite as accurate. For all the depths tested ranging from $d^* = 1mm$ to $d^* = 8mm$ we obtained accurate results. For depths past $8mm$, there was no readily identifiable criterion to predict *a priori* which depths could be estimated. Some estimates of d^* in the range $9mm$ to $20mm$ were good and some estimates would be considered only fair to poor. Full details can be found in [23]. Nonetheless, the results indicate the viability of this method in single parameter estimation problems.

5.2. Estimating Two Geometric Parameters

In Section 6 we discuss a need to modify the assumptions made in the original test problem to more accurately describe the behavior of *experimental* data obtained. In short, the computational domain was expanded beyond the edges of the sample and snapshots were taken of the magnetic flux density data *only* on a single line above the conducting sheet (instead of the whole region). For the computational trials in the 1-D case, we took snapshots of the magnetic vector potential for the

entire computational domain even though in the inverse problems we only used those data points along a *single* line. Furthermore, in dealing with experimental data we considered data across the entire length of the sample, instead of just half the sample as done in 1-D computational examples previously. We also implemented these changes in the two-parameter estimation problems.

Otherwise, we proceed as in the previous estimation problems by first generating an ensemble of damages. We consider damages with depths ranging from $1mm$ to $11mm$ in increments of $2mm$ in combination with lengths from $0.5cm$ to $3.5cm$ in increments of $1cm$ (we now consider longer damages similar to those in the next section involving experimental data). We keep the thickness fixed at $1mm$. A total of 24 snapshots, $\{B_2(d_i, l_j)\}$, $i = 1, ..., 6$, $j = 1, ..., 4$ were generated using Ansoft. We present results in Table 2 for estimating a depth of $d^* = 2mm$ and length $l^* = 1cm$, a depth of $d^* = 4mm$ and length $l^* = 2cm$, and finally a depth of $d^* = 6mm$ and length $l^* = 3cm$. (In each case, 10% relative noise was added to the generated data before use in the inverse problem criteria.)

Table 2. Results Estimating Two Parameters Simultaneously at a 10% Relative Noise Level

q	No. POD	True $\mathbf{q}^*$	Avg. Est. **q**	St. Dev.
depth	5	$2mm$	$2.0473mm$	$0.0045mm$
length	5	$1cm$	$1.0180cm$	$0.0087cm$
depth	5	$4mm$	$4.0850mm$	$0.0074mm$
length	5	$2cm$	$1.9801cm$	$0.0098cm$
depth	5	$6mm$	$6.0316mm$	$0.0031mm$
length	5	$3cm$	$3.0396cm$	$0.0055cm$

5.3. Conclusions

When using the B_2 field in the inverse problem, the methods proved to be accurate and robust, allowing us to accurately estimate the length, thickness, and depth of a damage within a sample as well as length and depth simultaneously even when the data contained considerable noise.

Furthermore, there are two significant findings to report with regard to the above results. First of all, in most cases *we were able to use 10 POD basis elements or less in each of the trials performed. We compare this to a total of over 7000 finite elements required to solve the boundary value problem initially* (using Ansoft Maxwell 2D Field Simulator). Hence, if one were to use the finite element software for each forward run, we could expect a time-intensive inverse problem. This leads us to the second, and most *significant*, finding with regard to reduction in computational time which can be summarized as follows. If one were to use a software package such as Ansoft's Maxwell 2D Field Simulator to calculate the forward problem each time it is required in the inverse problem, it would take approximately 5-7 minutes for a *single* forward solve and hence any inverse algorithm based on this forward solver may require several minutes to several *hours* of time for the optimization problem. In using the reduced order POD methodology for the forward problem, the

entire inverse problem takes approximately 8 seconds, less than $\frac{1}{40}$ the time required for a *single forward simulation*. As a forward algorithm is called numerous times, this is a substantial reduction in time required. For example, assuming an average of 20 iterative steps in the typical optimization procedure for these problems and a total forward simulation time of 5 minutes (300 seconds) to 7 minutes (420 seconds) for a finite element forward solve, the total computational time for the inverse problem would range from 1 hour 40 minutes (6000 seconds) to 2 hours 20 minutes (8400 seconds). Thus, we arrive at a speed up factor ranging from 750 to 1050, a factor of approximately 10^3.

Furthermore, most of the extensive computational time is required only in the initial collection of snapshots which would take place prior to implementation in a practical setting. This suggests that a *portable sensing device, when coupled with reduced order modeling in the inverse problem, might be plausible in practical damage detection applications.*

6. Experimental Results

The simulations performed in the previous section are most encouraging and suggest a natural next step to further test our proposed methods with experimental data. Therefore, we designed the experiment depicted in Figure 4, in which we try to detect and parameterize a damage within an aluminum sample using a giant magnetoresistive (GMR) sensor. The sample is constructed of 17
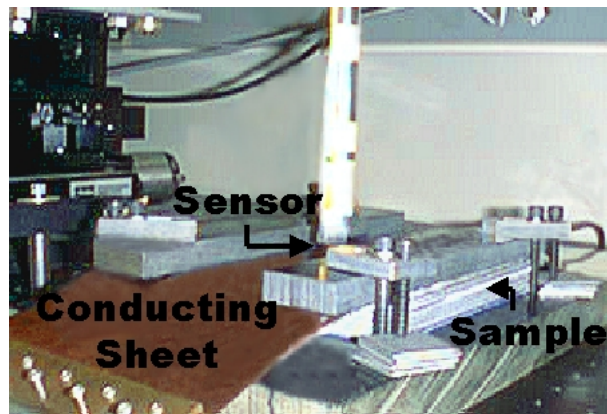
Figure 4. Experimental Setup

layers of $1mm$ thick aluminum plates with a slice cut out of one of the layers to simulate a damage within the sample (see Figure 5). The "damaged" piece of aluminum is moved from one layer to another to simulate damages within the sample at different depths, and the length of the damage is varied by producing "gaps" of varying size from the aluminum plate (the thickness of the damage is always fixed at $1mm$). As a means of inducing current within the sample, a thin sheet of copper carrying a uniform current of $3A$ is placed above the sample on top of a thin sheet of paper (to avoid direct physical contact between the sample and the conducting sheet). The GMR sensor measures the amplitude and phase of the magnetic flux density across a $2in$ line (along the length of the sample) every $0.635mm$. The data is then filtered through a lock-in amplifier and saved to a file.

Furthermore, we took data across various frequencies to analyze the effect of the frequency on the estimation problem.
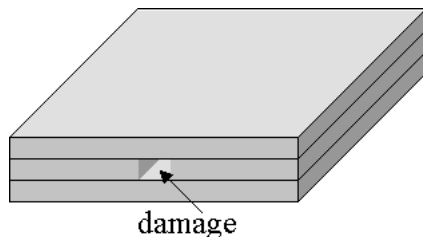

Figure 5. Schematic of the Damaged Layer

Frequency is a very important factor to consider when trying to detect and parameterize a damage. This is due to the depth of penetration of the eddy currents, also referred to as the "skin effect". Eddy currents are not uniformly distributed throughout a material but instead decay exponentially with depth in the material [40]. The distance at which the eddy current density has decreased by a factor of $1/e$ (36.8%) is called the *depth of penetration* and can be calculated by

$$\delta = \frac{1}{\sqrt{\pi f_s \mu \sigma}} \tag{52}$$

where f_s is the source frequency, μ is the magnetic permeability and σ is the conductivity of the material [10, p. 370]. We carried out experiments using four different frequencies, 250Hz, 500Hz, 1kHz and 2kHz with a depth of penetration ranging from $2.70mm$ to $7.64mm$ for 2kHz down to 250Hz, respectively. This provides varying sensitivity when considering damages at different depths.

Given the magnetic flux density data, $\hat{B}_2$, from the GMR sensor for a given damage at a specified depth d^* and with a given length l^*, we wished to estimate these parameters using an appropriate cost criterion. The first step in the optimization process was to generate snapshots representative of the experimental data across the various damages. To generate the snapshots, we first explored the idea of using simulations obtained from the finite element solver Ansoft Maxwell 2D Field Simulator to form the POD basis elements as done in the previous section. However, in order for the snapshots to be representative of the data, we needed to modify the assumptions made in the original test problem. We had originally assumed a sample of infinite length to disregard boundary effects from the edges of the material. Unfortunately, the experimental data showed significant boundary effects. Therefore, we modified the computational domain used in the finite element solver to that domain depicted in Figure 6 which includes the edges of the sample. Moreover, instead of only considering half of the sample, we now considered data across the entire length of the sample as collected in the experimental setup.

However, after analyzing the experimental data and the Ansoft simulations, we noticed significant differences between the data and simulations. (For details and analysis of these differences, see [23].) Consequently, we chose to instead snapshot directly on the experimental data to form the POD basis elements. Furthermore, to obtain a definite pattern in the data as a function of the damage within the sample, it was necessary to filter out the background noise (data obtained when the sample contained no damage) and to average the amplitude across the
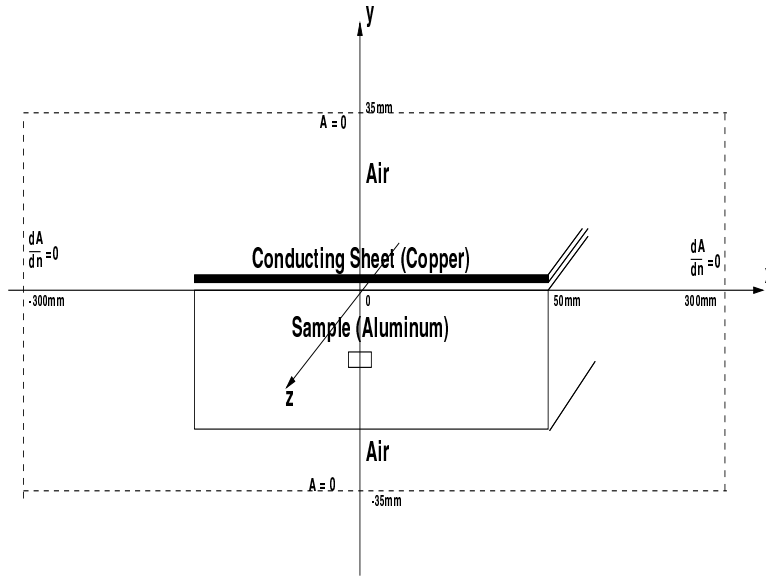
Figure 6. Modified Computational Domain

center of the damage (this produces desired symmetry in the data). However, while filtering out the background noise enhanced the differences in the data as a function of the various damages, at the same time, it also seemed to intensify the boundary effects present. Thus, it was necessary to disregard the data at the edges of the sample. In other words, we consider the cost function given by

$$J(\mathbf{q}) = \frac{1}{2} \sum_{j=a-2}^{b+2} \left| 10^9 B_2^N(x_j; \mathbf{q}) - 10^9 \hat{B}_2^j \right|^2, \tag{53}$$

where $\mathbf{q}$ is the vector containing the parameters we wish to estimate, $B_2^N(\mathbf{q})$ is the POD approximation formed using snapshots on the data itself, $\hat{B}_2^j$ is GMR data at grid points x_j, $j = 1, ..., n$ with n total grid points and a and b indicate the indices of the grid points we consider in our cost criterion.

In [23], we also analyzed the data when the phase data was manipulated with either a phase shift and/or when the phase data was averaged. We took data at different frequencies (the importance of which was mentioned above), and depending on the frequency, either the real portion of the data or imaginary portion of the data exhibited sporadic behavior. This was due, in part, to the phase of the data. If an appropriate phase shift was incorporated, the sporadic behavior of the data could be minimized. Furthermore, since it was necessary to average the amplitude across the center of the damage, it seemed logical to also consider averaging the phase data across the center of the damage. We performed extensive analysis of the data with these various modifications in [23] and concluded that the best results of the inverse problem, in all but one case considered (the case in which a source frequency of 1kHz was used), could be found when the data incorporated a phase shift. The phase shift seemed to intensify the variations in the data as a function of the damage within the sample. Furthermore, it was necessary to use only the real portion of the data or the

imaginary portion of the data in the cost criterion, but not both parts (due to the sporadic nature of the data as discussed above). The choice of either the real portion or imaginary portion could be readily determined by simply examining the data before implementation and determining which portion exhibited a clear pattern as opposed to sporadic behavior which would be found in the other portion of the data. In the case of 1kHz, a phase shift did not intensify the variation in the data as in the other cases but did just the opposite. As a consequence, for this frequency it was necessary to consider the data with no phase modifications.

Before presenting results for the inverse problems, we make one final note regarding the use of only a portion of the data in the cost criterion. To apply the results in a practical setting, it would be necessary to either develop a model which accurately portrays the data or to collect data over a period of time, building a data base which inherently contained the variations in the data. With this extensive data set, we would be able to discern the pattern in the data *a priori*. Thus, the frequency would indicate the appropriate form of the data to be used in the cost criterion.

Next, we present representative results below for the various frequencies, in which we use only the real portion of the data with a phase shift incorporated in the cost function given by (53) for frequencies 250Hz and 500Hz, the imaginary portion of the data with no phase shift is used in the cost function for frequency 1kHz and the imaginary portion of the data with a phase shift is used in the cost function for frequency 2kHz.

6.1. Determining the Length of the Damage

In determining the length of the damage, we kept the depth fixed at $2mm$ or $3mm$ and estimated a length of either $1cm$ or $1.5cm$ (keeping the thickness fixed at $1mm$). When estimating length, snapshots for the POD basis elements incorporated data from samples with damages at the fixed depth with varying lengths, *excluding* the true length. In other words, in trying to estimate a length of $1cm$ at a fixed depth of $2mm$, we used data from samples with damages having lengths of $0.5cm$, $1.5cm$, $2cm$ and $3cm$ all at a depth of $2mm$ to form the snapshots. In addition, all the POD basis elements were used in the approximation since we had only 4 basis elements. (Only a small amount of data was taken to establish proof-of-concept.) The results of the estimation problem can be found in Table 3 (where '-' indicates that the optimization routine failed to converge to an estimated parameter).

6.2. Determining the Depth of the Damage

In determining the depth of the damage, we analyzed the results obtained when detecting the same depth using various frequencies at a fixed length of $1cm$ and $1.5cm$. In forming the snapshots, we did the same as with length where our snapshots were given by magnetic flux density data for samples with damages with the chosen fixed length (and fixed thickness of $1mm$) at all the depths ($1mm$, $2mm$, $3mm$, $4mm$, $6mm$, and $8mm$) *excluding* the depth we wish to estimate. Tables 4 and 5 summarize the results.

Table 3. Determination of Length

Frequency (Hz)	Depth (*mm*)	Actual Length (*cm*)	Optimized Length (*cm*)	Relative Error
250	2	1.0	1.5068	50.68%
		1.5	2.5713	71.42%
	3	1.0	0.9254	7.46%
		1.5	1.3869	7.54%
500	2	1.0	0.8002	19.98%
		1.5	1.6036	6.91%
	3	1.0	0.9225	7.75%
		1.5	1.5540	3.60%
1000	2	1.0	0.8169	18.31%
		1.5	1.4789	1.41%
	3	1.0	-	-
		1.5	-	-
2000	2	1.0	0.7566	24.34%
		1.5	2.7050	80.34 %
	3	1.0	1.3782	37.82%
		1.5	1.3100	12.67 %

Table 4. Determination of Depth with Fixed Length 1.0*cm*

Actual Depth(mm)	Frequency(Hz)	Optimized Depth(mm)	Relative Error
2	250	0.9411	52.95%
	500	2.1919	9.59%
	1000	2.1191	5.96 %
	2000	2.0479	2.39 %
3	250	3.4827	16.09%
	500	2.8047	6.51 %
	1000	2.9004	3.32 %
	2000	2.9127	0.91 %

6.3. Determining the Length and Depth of the Damage

In our final trials, we estimated both length and depth simultaneously. In order to implement the interpolation routine for our POD approximation of the magnetic flux density, we need to have a grid upon which we know the values of our coefficients for our POD approximations. However, in forming our snapshots for a specific estimation, we *exclude all the data with either the same depth*

Table 5. Determination of Depth with Fixed Length 1.5*cm*

Actual Depth(mm)	Frequency(Hz)	Optimized Depth(mm)	Relative Error
2	250	1.5721	21.40%
	500	1.8979	5.10 %
	1000	1.8330	9.35 %
	2000	1.6484	17.58%
3	250	-	-
	500	3.1094	3.15%
	1000	3.1274	4.25%
	2000	3.2070	6.90%

or length as that we are attempting to estimate. For example, if we are estimating a length of $l^* = 1.5cm$ and a depth of $d^* = 2mm$, our snapshots consist of data for samples with damages having lengths 0.5*cm*, 1*cm*, 2*cm* and 3*cm* at depths 1*mm*, 3*mm*, 4*mm*, 6*mm* and 8*mm* (all with fixed thickness of 1*mm*). In this case, we only analyze the results using a frequency of 500Hz. The results can be found in Table 6.

Table 6. Determination of Depth *and* Length Simultaneously with Frequency 500Hz

		Actual Length l	
		1cm	1.5cm
Actual Depth d	2mm	$l = 1.0635$ $d = 2.3097$	$l = 1.8080$ $d = 1.8403$
	3mm	$l = 0.9065$ $d = 2.9522$	$l = 1.4612$ $d = 2.9759$

6.4. Conclusions

Assuming a fixed source frequency and its associated cost criterion, we were able to demonstrate that the POD method in the context of inverse problems is a viable method even with experimental data. Depending on the frequency used, we were able to quite accurately estimate the length and depth alone. Estimating the two parameters simultaneously was a little more challenging; however, we still obtained reasonable results. In estimating length alone, using either 500Hz with the phase shifted or 1kHz with raw phase produced accurate results when comparing data across all the data points across the center of the damage. In a few cases using 250Hz or 2kHz also produced fairly accurate; however, results using these frequencies were not consistent. In determining the depth of the damage alone, frequencies 500Hz, 1kHz and 2kHz again produced accurate results for the depths estimated with less than 10% error. Our tests suggest that 250Hz is not a viable

frequency for interrogation in any case presented in this paper. When estimating length and depth simultaneously, using 500Hz produced accurate results in many cases. Overall, the methods again proved to be feasible when used with experimental data.

In some cases, depending on the length or depth of the damage, certain frequencies were found to be more accurate than others; therefore, the most accurate results may be found by using the reduced order POD methodology together with another NDE technique. For example, the magneto-optic/eddy current imager ([16, 45]) is a visually based technique which displays crack images or images of the magnetic fields surrounding the actual crack. An estimate of the crack length may be obtained from these images giving us *a priori* knowledge of the damage. Based upon these estimates, a source frequency as well as an initial guess for the optimization routine can be chosen, providing valuable information for use in the inverse problem.

In conclusion, given the data available, we have shown we can *successfully* use our proposed reduced order computational methodology to determine both the length and depth of a damage within a sample (both separately and simultaneously). Moreover, since we only used a few basis elements (due to the small sample size), the results were obtained quite quickly, giving us a method which is both fast and accurate on experimental data. Indeed this section gives concrete results indicating that the POD methodology in the context of appropriate least squares techniques is a practical approach to nondestructive damage detection.

7. Concluding Remarks

In this paper, we developed a model for a specific eddy current method making some simplifying assumptions reducing the three-dimensional problem to a two-dimensional problem. We utilized a mathematical tool (phasors) where complex valued fields were employed allowing us to suppress the time-dependence. Furthermore, for computational purposes, we included two additional quantities in the Maxwell formulations, a magnetic vector potential and a scalar electric potential, deriving the boundary value problem for the magnetic vector potential with some additional constraints on the electric scalar potential. Given the magnetic vector potential, we could easily derive the magnetic flux density necessary for the parameter estimation problem.

We then presented some theoretical results which established the existence and uniqueness of solutions as well as continuous dependence of the solution on the parameters which represent the damage. We further discussed theoretical issues concerning the least squares parameter estimation problem used to identify the geometry of the damage.

Since the parameter estimation problem involves solving the forward problem numerous times, we needed extremely fast and accurate solution methods. Therefore, in Section 4, we discussed the reduced order POD method which allows one to create a set of basis elements spanning a data set consisting of either numerical simulations or experimental data. The POD method is unique in that the majority of information is captured in just a few basis elements, allowing us to use a smaller number of basis elements for each forward solution. This results in a substantial decrease in total computational time. We also discussed two different approaches in forming the POD approximation, a POD/Galerkin technique and a POD/Interpolation technique and concluded that in *this* problem,

the POD/Interpolation method gave a much better approximation than the POD/Galerkin method. Furthermore, using only three basis elements with the POD/Galerkin method we still obtained an approximation with less than a 7% relative error when compared to a finite element solution using more than 7000 finite elements. Using the POD/Interpolation method, we achieved less than a 1% relative error using four or more POD basis elements.

In Section 5, we presented parameter estimation results when estimating one or two parameter values using simulated data. In both cases, we were able to achieve extremely accurate results even with 10% relative noise added. In addition, on average we obtained a total reduction in time of a factor of approximately 10^3.

Finally, we offered results of the parameter estimation problem when using experimental data obtained from a giant magnetoresistive (GMR) sensor. The experimental results were based on successfully using actual experimental data to form the POD basis elements (instead of numerical simulations) and thus illustrated the effectiveness of this method on a wide range of applications. In other words, whenever it is difficult to model the physical process but "good" data is available, the POD method may be a viable option. Taken as a whole, our work here indicates that using a POD computational method in NDE research can be an attractive alternative to the standard finite element methods, offering the potential for substantial savings in total computational time.

Acknowledgments

References

[1] Ansoft Corporation. *Maxwell 2D Field Simulator - Technical Notes*, 1995-1999.

[2] H.T. Banks, R.C. del Rosario, and R.C. Smith. Reduced order model feedback control design: Numerical implementation in a thin shell model. *IEEE Trans. Auto. Control*, 45:1312–1324, July 2000.

[3] H.T. Banks, M.L. Joyner, B. Wincheski, and W.P. Winfree. Evaluation of material integrity using reduced order computational methodology. CRSC Tech. Rep. CRSC-TR99-30, North Carolina State University, 1999.

[4] H.T. Banks, M.L. Joyner, B. Wincheski, and W.P. Winfree. Nondestructive evaluation using a reduced-order computational methodology. *Inverse Problems*, 16:929–945, 2000.

[5] H.T. Banks, R.C. Smith, and Y. Wang. *Smart Material Structure: Modeling, Estimation, and Control*. Masson/J. Weiley, Paris/Chichester, 1996.

[6] G. Berkooz. Observations on the proper orthogonal decomposition. In *Studies in Turbulence*, pages 229–247. Springer-Verlag, New York, 1992.

[7] G. Berkooz, P. Holmes, and J.L. Lumley. The proper orthogonal decomposition in the analysis of turbulent flows. *Annual Review of Fluid Mechanics*, 25(5):539–575, 1993.

[8] Don E. Bray. *Nondestructive Testing Techniques*. John Wiley & Sons, New York, 1992.

[9] Louis Cartz. *Nondestructive Testing*. ASM International, Materials Park, OH, 1995.

[10] David K. Cheng. *Field and Wave Electromagnetics*. Addison-Wesley, Reading, MA, second edition, 1992.

[11] A. Cochran, G.B. Dondaldson, C. Carr, D. McA. McKirdy, M.E. Walker, U. Klein, J. Kuznik, and A. McNab. Advances in the theory and practice of SQUID NDE. *Review in Progress in QNDE*, 15:1151–1158, 1996.

[12] R.C. del Rosario. *Computational Methods for Feedback Control in Structural Systems.* PhD thesis, North Carolina State University, 1998.

[13] G.B. Donaldson and D. McA. McKirdy. The use of SQUIDs for nondestructive evaluation. In *SQUID Sensors: Fundamentals, Fabrication and Application,* pages 599–628. Kluwer Academic Publishing, Boston, 1996.

[14] Robert S. Elliott. *Electromagnetics: History, Theory, and Applications.* IEEE Press, New York, 1993.

[15] Lawrence C. Evans. *Partial Differential Equations.* American Mathematical Society, Providence, 1991.

[16] G.L. Fitzpatrick, D.K. Thorne, R.L. Skaugset, E.Y.C. Shih, and W.C.L. Shih. Magneto-optic/eddy current imaging of aging aircraft: A new NDI technique. *Materials Evaluation,* 51:1402–1407, 1993.

[17] T.W. Guettinger, K. Grotz, and H. Wezel. Eddy current imaging. *Materials Evaluation,* 51:444–451, April 1993.

[18] R. Halmshaw. *Non-Destructive Testing.* Edward Arnold, London, second edition, 1991.

[19] N.C. Haywood and J.R. Bowler. Eddy-current imaging of buried cracks by inverting field data. *IEEE Trans. On Magnetics,* 28(2):1336–1339, 1992.

[20] C. A. Hogarth and J. Blitz, editors. *Techniques of Non-Destructive Testing.* Butterworths, London, 1960.

[21] J. D. Jackson. *Classical Electrodynamics.* John Wiley & Sons, New York, 2nd edition, 1975.

[22] W.G. Jenks and J.P. Wikswo Jr. Review article: SQUIDs for nondestructive evaluation. *Journal of Physics D: Applied Physics,* 30:293–323, 1997.

[23] Michele L. Joyner. *An Application of a Reduced Order Computational Methodology for Eddy Current Based Nondestructive Evaluation Techniques.* PhD thesis, North Carolina State University, 2001.

[24] K. Karhunen. Zur spektral theorie stochasticher prozesse. *Ann. Acad. Sci. Fennicae,* 37(A1), 1946.

[25] C.T. Kelley. *Iterative Methods for Optimization.* Society for Industrial and Applied Mathematics, Philadelphia, PA, 1999.

[26] M. Kirby, J.P. Boris, and L. Sirovich. A proper orthogonal decomposition of a simulated supersonic shear layer. *International Journal for Numerical Methods in Fluids,* 10:411–428, 1990.

[27] M. Kirby and L. Sirovich. Application of the Karhunen-Loeve procedure for the characterization of human faces. *IEEE Transactions on Pattern Analysis and Machine Intelligence,* 12(1):103–108, 1990.

[28] A. Konrad. Integrodifferential finite element formulation of two-dimensional steady-state skin effect problems. *IEEE Transactions on Magnetics,* 18(1):284–292, 1981.

[29] A. Konrad. The numerical solution of steady-state skin effect problems - an integrodifferential approach. *IEEE Transactions on Magnetics,* 17(1):1148–1152, 1981.

[30] Andrzej Krawczyk and John A. Tegopoulos. *Numerical Modelling of Eddy Currents.* Oxford University Press, Oxford, 1993.

[31] E. E. Kriezis, Theodoros D. Tsiboukis, Stavros M. Panas, and Jon A. Tegopoulos. Eddy currents: Theory and applications. *Proceedings of the IEEE,* 80(10):1559–1589, 1992.

[32] K. Kunisch and S. Volkwein. Control of Burgers' equation by a reduced-order approach using proper orthogonal decomposition. *J. Optimization Theory and Applic.,* 102(2):345–371, 1999.

[33] M. Loeve. Functions aleatoire de second ordre. *Compte rend. Acad. Sci. Paris,* 1945.

[34] J.L. Lumley. The structure of inhomogeneous turbulent flows. *Atmospheric Turbulence and Radio Wave Propagation,* pages 166–178, 1967.

[35] J.L. Lumley. *Stochastic Tools in Turbulence.* Academic Press, New York, 1970.

[36] H.V. Ly and H.T. Tran. Proper orthogonal decomposition for flow calculations and optimal control in a horizontal CVD reactor. CRSC Tech. Rep. CRSC-TR98-13, North Carolina State University, 1998, *Quart. Appl. Math,* to appear.

[37] Y.P. Ma and Jr. J.P. Wikswo. Imaging subsurface defects using a SQUID magnetometer. *Review of Progress in QNDE,* 12A:1137–1143, 1993.

[38] Warren J. McGonnagle. *Nondestructive Testing.* McGraw-Hill, New York, 1961.

[39] D. McA. McKirdy, A. Cochran, G.B. Donaldson, and A. McNab. Forward and inverse processing in electromagnetic NDE using SQUIDs. *Review of Progress in QNDE,* pages 347–354, 1996.

[40] Patrick O. Moore and Paul McIntire, editors. *Nondestructive Testing Overview,* volume Ten of *Nondestructive Testing Hanbook.* American Society for Nondestructive Testing, Inc., second edition, 1996.

[41] J.A. Nelder and R. Mead. A simplex method for function minimization. *Comput. J.*, 7:308–313, 1965.

[42] Alfio Quarteroni, Riccardo Sacco, and Fausto Saleri. *Numerical Mathematics*. Springer-Verlag, New York, 2000.

[43] J. Stoer and R. Burlisch. *Introduction to Numerical Analysis*. Springer-Verlag, New York, 2nd edition, 1993.

[44] Richard L. Stoll. *The Analysis of Eddy Currents*. Clarendon Press, Oxford, 1974.

[45] D.K. Thorne, G.L. Fitzpatrick, E.Y.C. Shih, and W.C.L. Shih. Aircraft inspection with the magneto-optic/eddy current imager - a new technology. In *ATA NDT Forum*, Long Beach, CA, Sept. 1991.

[46] I.A. Tsukerman, A. Konrad, and J.D. Lavers. A method for circuit connections in time-dependent eddy current problems. *IEEE Transactions on Magnetics*, 28(2):1299–1302, 1992.

[47] J. Weiss and Z. J. Csendes. A one-step finite element method for multiconductor skin effect problems. *IEEE Transactions on Power Apparatus and Systems*, 101(10):3796–3803, 1982.

[48] H. Wienstock. A review of SQUID magnetometry applied to nondestructive evaluation. *IEEE Transactions on Magnetics*, 27(2):3131–3236, 1991.

[49] B. Wincheski, J. Fulton, S. Nath, M. Namking, and J. Simpson. Self-nulling eddy current probe for surface and subsurface flaw detection. *Materials Evaluation*, 52(1):22–26, 1994.

[50] B. Wincheski, J. Fulton, S. Nath, and M. Namkung. Analysis of eddy current distribution and resulting flaw detection mechanism for self-nulling probe. *Review of Progress in Quantitative NDE*, 14A:291–298, 1995.

[51] Buzz Wincheski and Min Namkung. Development of very low frequency self-nulling probe for inspection of thick layered aluminum structures. In *1998 Review of Progress in Quantitative NDE*, Snowbird, Utah, Aug. 1998.

[52] Buzz Wincheski and Min Namkung. Deep flaw detection with giant magnetoresistive (GMR) based self-nulling probe. In *1999 Review of Progress in Quantitative NDE*, Montreal, Canada, July 1999.

[53] J. Wloka. *Partial Differential Equations*. Cambridge University Press, Cambridge, 1987.